Journal of
Sensor and Actuator Networks

MDPI

Article

Robust Distributed Collaborative Beamforming for WSANs in Dual-Hop Scattered Environments with Nominally Rectangular Layouts

Oussama Ben Smida [1,*], Sofiène Affes [1,*], Dushantha Jayakody [2,3,4] and Yoosuf Nizam [5]

[1] EMT Centre, INRS, University of Quebec, Montreal, QC H5A 1K6, Canada
[2] COPELABS, Lusofona University, 1749-024 Lisbon, Portugal; dushantha.jayakody@ulusofona.pt
[3] Center of Technology and Systems (UNINOVA-CTS) and Associated Lab of Intelligent Systems (LASI), 2829-516 Caparica, Portugal
[4] CIET/DEEE, Faculty of Engineering, Sri Lanka Institute of Information Technology, Colombo 10115, Sri Lanka
[5] Faculty of Engineering, Science, and Technology, The Maldives National University, Sosunge, Sosunmagu, Malé 20068, Maldives; yoosuf.nizam@mnu.edu.mv
* Correspondence: oussama.ben.smida@inrs.ca (O.B.S.); sofiene.affes@inrs.ca (S.A.)

Abstract: We introduce a robust distributed collaborative beamforming (RDCB) approach for addressing channel estimation challenges in dual-hop transmissions within wireless sensor and actuator networks (WSANs) of K nodes. WSANs enhance wireless communication by reducing data transmission, latency, and energy consumption while optimizing network load through integrated sensing and actuation. The source S transmits signals to the WSAN, where nodes relay them to the destination D using beamforming weights to minimize noise and preserve signal integrity. These weights depend on channel state information (CSI), where estimation errors degrade performance. We develop RDCB solutions for three first-hop propagation scenarios—monochromatic [line-of-sight (LoS)] or "M", bichromatic (moderately scattered) or "B", and polychromatic (highly scattered) or "P"—while assuming a monochromatic LoS or "M" link for the second hop between the nodes and the far-field destination. Termed MM-RDCB, BM-RDCB, and PM-RDCB, respectively ("X" and "Y" in XY-RDCB—for $X \in \{M, B, P\}$ and $Y \in \{M\}$—refer to the chromatic natures of the first- and second-hop channels, respectively, to which a specific RDCB solution is
tailored), these solutions leverage asymptotic approximations for large K values and the nodes' geometric symmetries. Our distributed solutions allow local weight computation, enhancing spectral and power efficiency. Simulation results show significant improvements in the signal-to-noise ratio (SNR) and robustness versus WSAN node placement errors, making the solutions well suited for emerging 5G and future 5G+/6G and Internet of Things (IoT) applications for different challenging environments.

Keywords: distributed collaborative beamforming (DCB); robust DCB (RDCB); wireless sensor and actuator network (WSAN); deterministic WSAN; geometrical grids; angular spread (AS); synchronization; localization; channel mismatch; 5G+/6G; IoT

Academic Editors: Dionisis Kandris, Eleftherios Anastasiadis and Purav Shah

Received: 29 January 2025
Revised: 9 March 2025
Accepted: 11 March 2025
Published: 19 March 2025

Citation: Ben Smida, O.; Affes, S.; Jayakody, D.; Nizam, Y. Robust Distributed Collaborative Beamforming for WSANs in Dual-Hop Scattered Environments with Nominally Rectangular Layouts. *J. Sens. Actuator Netw.* **2025**, *14*, 32. https://doi.org/10.3390/jsan14020032

1. Introduction

A wireless sensor–actuator network (WSAN) is a network of sensors and actuators linked by wireless communication. Sensors are typically compact, stationary devices with constrained power and computational capabilities, responsible for monitoring the surrounding environment. Actuators, in contrast, are resource-rich devices that can move and

carry out appropriate actions or control devices based on the data collected. In WSANs, sensors and actuators work together: sensors gather environmental data, while actuators process this information to make decisions and respond effectively [1]. WSANs are applicable in various fields, including environmental monitoring, battlefield surveillance, space missions, etc., where timely responses to detected events are crucial. These networks are also vital in sectors requiring continuous monitoring and control, such as smart grids, automated industrial systems, and precision agriculture. However, WSANs face limitations, including restricted energy resources, bandwidth constraints, and the need for reliable, real-time communication, particularly in dynamic or complex settings [1–4].

Collaborative beamforming (CB) is an effective strategy for enhancing transmission range, connection reliability, and network capacity in wireless sensor networks [5–12]. In this approach, K autonomous sensor nodes work together to relay information between a source–destination pair (S, D) via two-hop communication by assessing and transmitting weighted copies of the desired signal during two time slots. CB is applicable across various fields, including environmental monitoring, agriculture, remote sensing, healthcare, safety, transportation, smart homes, entertainment, defense, and crisis management. Its versatility has drawn the attention of researchers, expanding its use from line-of-sight to more complex scattered environments [5,9–12]. CB thus addresses some key limitations of WSANs, such as interference management, energy constraints, and the need for reliable, real-time communication.

However, implementing CB necessitates prior knowledge of all other nodes' information, resulting in significant data exchange among nodes. To tackle this shortcoming, distributed CB (DCB) solutions can be developed by relying solely on the information locally available at each node, enabling an approximation of the optimal beamforming weights. Recent advances have further refined decentralized beamforming techniques, improving frequency alignment and increasing network robustness [13–15].

Despite this, the effectiveness of beamforming weights hinges on the accuracy of locally estimated or fed-back channel state information (CSI) parameters, with potential errors that can degrade performance. Several studies [16–27] have introduced robust CB (RCB or RDCB) approaches to mitigate these errors, categorized into worst-case and stochastic approaches. These methods either deal with maximum error scenarios—often proving inefficient in real-world situations—or rely on iterative greedy algorithms that explore numerous potential solutions, which can overwhelm the computational and power resources of WSAN nodes. Recent studies have explored alternative robust beamforming strategies that balance performance with computational efficiency [20,22]. Moreover, novel approaches use distributed beamforming to reconnect separated sensor nodes in mobile networks and conceal base station locations, improving network robustness and security against tracking and interference [14,28].

Existing beamforming techniques face high computational complexity, limiting real-time use in large-scale systems. Scalability challenges arise as managing multiple nodes increases system complexity. Thus, this work (supported by the Discovery Grants (DGs) and CREATE PERSWADE (<www.create-perswade.ca>) Programs of NSERC) aims to develop RDCB solutions that effectively address channel node placement errors with minimal overhead, computation, and power costs. We specifically seek new solutions for structured WSANs with deterministic spatial distributions as opposed to unstructured WSANs, which have random spatial arrangements [29,30]. In structured WSANs, nodes are strategically placed to enhance coverage, resulting in lower costs and easier maintenance compared to unstructured networks [29,30]. For instance, structured WSANs are well suited for multimedia applications requiring affordable sensors equipped with cameras and microphones, arranged to optimize coverage for collecting and processing audio, video,

and image data. In contrast, unstructured WSANs randomly place nodes, complicating tasks like connectivity, failure detection, and network management [29,30]. Such networks are more prone to connectivity issues due to their random configurations, making effective management challenging. To enhance connectivity in these environments, mobile nodes may be utilized. In this work, we concentrate on the advantages of structured WSANs, leveraging their potential for wide coverage at a low cost.

We introduce an RDCB solution designed to address significant channel estimation issues in dual-hop transmissions across a WSAN with K nodes arranged in a nominally rectangular or square layout. The process begins with the source S transmitting its signal to the WSAN. WSANs achieve higher efficiency in wireless communications by minimizing data transmission, reducing latency, conserving energy, and optimizing network loads through the integration of both sensing and actuation capabilities, making it optimal in our application. After receiving the signal, each node transmits it to the destination D, applying a selected beamforming weight to minimize noise power and ensure that the desired signal remains equal to unity at D. The selected weights rely on CSI parameters, necessitating local estimation or feedback at each node, which can lead to estimation or feedback errors, thereby degrading the DCB performance.

In light of the extensive connectivity offered by emerging 5G and future 5G+/6G technologies, along with the IoT, we propose alternative RDCB strategies that are adaptable to various propagation scenarios, including monochromatic (LoS), bichromatic (slightly to moderately scattered), and polychromatic (highly scattered) ones, during the first hop, with an LoS link assumed for the second hop. In [31], we developed preliminary RDCB designs that are suitable for slightly to moderately scattered scenarios. (This article is a revised and expanded version of a paper entitled "Dual-Hop Robust Distributed Collaborative Beamforming Over Nominally Rectangular WSNs in Slightly to Moderately Scattered Environments", which was presented at the IEEE IWCMC 2023, Marrakesh, Morocco, 19–23 June 2023.) In this paper, we further extend that work by developing new RDCB solutions that perfectly cope with more complex and practical environments as well. Referred to as MM-RDCB, BM-RDCB, and PM-RDCB for the mono-, bi-, and polychromatic cases, respectively, they utilize highly efficient asymptotic approximations for a large number of nodes, K, and exploit the geometric symmetries present in their rectangular or square configurations. Furthermore, they are designed to be distributed, enabling each terminal to locally compute its weights. This significantly enhances both spectral and power efficiency within the WSAN. Our RDCB approach enhances robustness by mitigating CSI estimation errors without high computational costs. It improves computational efficiency through asymptotic approximations, making it ideal for large-scale WSANs, and ensures scalability by leveraging WSAN structures. Simulation results indicate notable improvements in the signal-to-noise ratio (SNR) and increased resilience to errors in node placement.

The structure of this paper is the following: Section 2 outlines the system model for dual-hop source-to-destination communication in a WSAN. Section 3 presents the proposed RDCB techniques. Simulation results are discussed in Sections 4, followed by concluding remarks in Section 5.

Notation : Bold uppercase and lowercase letters represent matrices and column vectors, respectively. $[.]_i$ and $[.]_{il}$ are the i^{th} entry of a vector and $(i,l)^{th}$ entry of a matrix, respectively. The operators $(.)^*$, $(.)^T$, and $(.)^H$ denote the complex conjugate, the transpose, and the complex conjugate transpose or Hermitian, respectively. $Tr(.)$ is the trace of a matrix. The operator $||.||$ represents the two-norm of a vector, whereas $|.|$ denotes the absolute value. The symbol $\odot$ indicates the element-wise product. $E\{.\}$ expresses the the statistical expectation, and $J_1(.)$ stands for the first-order Bessel function of the first kind. To assist the reader, Table 1 provides the definitions of the most commonly used acronyms in this paper.

Table 1. Relevant abreviations.

AoA	Angle of arrival
AoD	Angle of departure
AS	Angular spread
ASANR	Average-signal-to-average-noise ratio
ASNR	Average signal-to-noise ratio
BM	Bichromatic–monochromatic
CB	Collaborative beamforming
CSI	Channel state information
DCB	Distributed collaborative beamforming
LoS	Line of sight
MM	Monochromatic–monochromatic
PM	Polychromatic–monochromatic
RDCB	Robust distributed collaborative beamforming
SNR	Signal-to-noise ratio
WSAN	Wireless sensor and actuator network

2. System Model

As shown in Figure 1, we are examining a system that features a WSAN with K hybrid nodes (sensors/actuators), each possessing a single isotropic antenna both at the transmit and receive sides, that are capable of sensing and collecting data, have computational and actuation capabilities, and are able to transmit/receive different signals. The nodes are positioned with inter-distances of d_1 and d_2 along the x and y axes, respectively, and are uniformly arranged in a rectangular (i.e., $K = K_1 \times K_2$) or square grid (i.e., $K_1 = K_2 = K_0$; $K = K_0^2$; and $d_1 = d_2 = d_0$). The configuration includes a reference center, O, a source, S, and a destination, D, all located on a single plane (2D representation). Assuming that S and D are significantly separated, the cluster of K WSAN nodes operates in the far field relative to each terminal, enabling data relaying through a dual-hop communication scheme, S-WSAN-D, or otherwise, D-WSAN-S (i.e., by reciprocity). In the remainder of this paper, we assume without loss of generality that D is the one located in the far field relative to the WSAN.

Let the pair (A_S, ϕ_S) represent the polar coordinates of the source S, with s being its narrow-band unit-power signal, and let the polar coordinates of the destination D be (A_D, ϕ_D). Since the WSAN is assumed to operate in the far field relative to both terminals, A_S and A_D must be both significantly larger than the physical dimensions of the WSAN, $K_1 d_1$ and $K_2 d_2$, meaning that $A_* \gg K_i d_i$ for $* \in S, D$ and $i \in 1, 2$.

For simplicity, the source S is positioned at $\phi_S = 0$. The coordinates of the k-th node, $\equiv (k_1, k_2)$, are represented in polar form as (r_k, ψ_k) and in Cartesian form as $[k_1 d_1, k_2 d_2]^T$. It can be easily verified that $\psi_k = \arctan\left(\frac{k_2 d_2}{k_1 d_1}\right)$ and $r_k = \sqrt{(k_1 d_1)^2 + (k_2 d_2)^2}$. As noted earlier, this work considers potential placement errors for the nodes, defined in terms of the Cartesian coordinates as $d_1 \delta_{k_1}$ and $d_2 \delta_{k_2}$, both assumed to be independent and uniformly distributed, with variances of $d_1^2 \sigma_x^2$ and $d_2^2 \sigma_y^2$ along the x and y axes, respectively.

Additionally, let $[\mathbf{g}]_k$, $[\mathbf{g}]_{p,k}$ and $[\mathbf{f}]_k$ represent the desired backward, the interfering backward, and the forward channels, respectively, where $k = k_1 + (K_1 + 1)/2 + K_1 \times (k_2 + (K_2 - 1)/2)$ for $k_1 = \frac{-K_1+1}{2}, \frac{-K_1+3}{2}, \ldots, \frac{K_1-1}{2}$ and $k_2 = \frac{-K_2+1}{2}, \frac{-K_2+3}{2}, \ldots, \frac{K_2-1}{2}$.

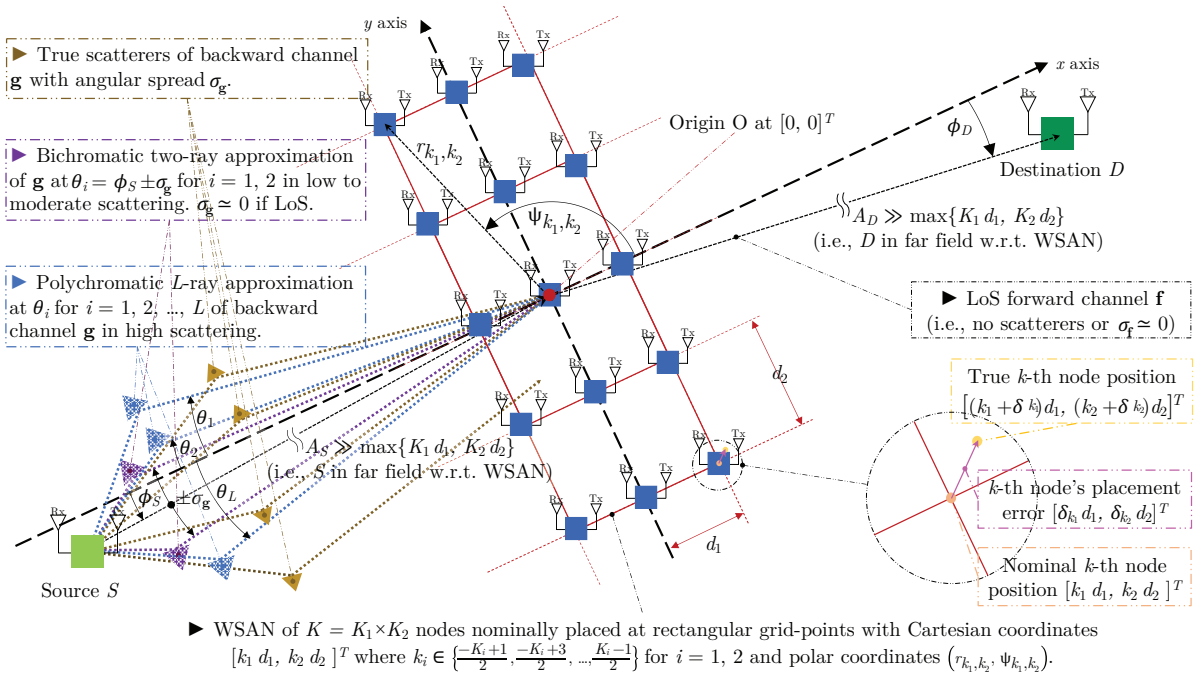

Figure 1. System model.

We consider that scattering over the S-WSAN hop, characterized by the angular spread (AS) σ_g, can be classified into the following scenarios: (i) negligible with $\sigma_g \simeq 0$ (i.e., LoS or monochromatic), in which case it can be approximated by a single ray with a complex gain, $\alpha = \rho exp(i\theta)$, where θ is uniformly distributed over $[-\pi, \pi]$ and originates from the angle Φ_S; (ii) slight to moderate with $\sigma_g \leq 20$ degrees when it can to be modeled as bichromatic propagation involving two equal-power rays having complex gains, $\alpha_i = \rho_i \exp(j\theta_i)$, for $i \in 1, 2$, where ρ_i represents two equal-power amplitudes satisfying $\mathbb{E}[\rho_i]^2 = \frac{1}{2}$ and θ_i is uniformly distributed over $[-\pi, \pi]$ and originates from the angles $\phi_i = \phi_S \pm \sigma_g$ [9,32]; or (iii) high with $\sigma_g > 20$ degrees when it can be well approximated by polychromatic propagation [11] involving L equal-power rays with complex gains, $\alpha_i = \rho_i \exp(j\theta_i)$, for $i \in 1, 2, \ldots, L$, where ρ_i represents L equal-power amplitudes with $\mathbb{E}[\rho_i]^2 = \frac{1}{L}$ and θ_i is uniformly distributed over $[-\pi, \pi]$ and originates from the angles ϕ_is uniformly distributed over $\left[\Phi_S - \sqrt{3}\sigma_g, \Phi_S + \sqrt{3}\sigma_g\right]$ such that $\sigma_g < \pi/\sqrt{3}$. As mentioned earlier, we assume that scattering over the WSAN-D hop is always negligible with $\sigma_f \simeq 0$ since D is located in the far field relative to the WSAN. Additionally, we assume that all WSAN nodes experience identical path loss over both the backward and forward hops. Accordingly, the model conforms to the framework of phased arrays.

In this work, as the WSAN nodes are assumed to function independently from a "communications" standpoint, each k-th WSAN node has knowledge solely of its own nominal Cartesian location coordinates and has no knowledge of the locations of other nodes in the WSAN. The only shared CSI among the nodes consists of nominal global parameters values that characterize the entire WSAN and its dual-hop propagation environment. These parameters include the grid distances d_1 and d_2, the grid dimensions K, K_1, and/or K_2, the AoA from the source S ϕ_S, the AoD to the destination D ϕ_D, the AS σ_g, the wavelength λ, the angle ϕ_l, and the complex gains α_l of the backward channel g when scattering occurs during the first hop. Additionally, they share the normalized location error variances σ_x^2 and σ_y^2 when implementing RDCB solutions.

Based on its knowledge of these parameters with a given accuracy, each WSAN node with the index $k \equiv (k_1, k_2)$ is capable of independently and locally reconstructing its

nominal backward and forward channel coefficients (i.e., without any communication with other nodes) as follows:

$$\begin{aligned}[\bar{\mathbf{g}}]_k &= \sum_{l=1}^{L} \alpha_l \exp\left(-j\frac{2\pi}{\lambda} r_k \cos(\phi_l - \psi_k)\right) \\ &= \sum_{l=1}^{L} \alpha_l \exp\left(-j\left(\frac{2\pi}{\lambda}(|k_1| d_1 \cos(\phi_l) + k_2 d_2 \sin(\phi_l))\right)\right), \end{aligned} \tag{1}$$

and

$$\begin{aligned}[\bar{\mathbf{f}}]_k &= \exp\left(-j\frac{2\pi}{\lambda} r_k \cos(\phi_D - \psi_k)\right) \\ &= \exp\left(-j\left(\frac{2\pi}{\lambda}(|k_1| d_1 \cos(\phi_D) + k_2 d_2 \sin(\phi_D))\right)\right). \end{aligned} \tag{2}$$

In environments with slight to moderate scattering, it should be noted that (1) simplifies to

$$\begin{aligned}[\bar{\mathbf{g}}]_k &= \alpha_1 \exp\left(-j\frac{2\pi}{\lambda} r_k \cos(\sigma_{\mathbf{g}} - \psi_k)\right) + \alpha_2 \exp\left(-j\frac{2\pi}{\lambda} r_k \cos(\sigma_{\mathbf{g}} + \psi_k)\right) \\ &= \alpha_1 \exp\left(-j\left(\frac{2\pi}{\lambda}(|k_1| d_1 \cos(\sigma_{\mathbf{g}}) + k_2 d_2 \sin(\sigma_{\mathbf{g}}))\right)\right) + \alpha_2 \exp\left(-j\left(\frac{2\pi}{\lambda}(|k_1| d_1 \cos(\sigma_{\mathbf{g}}) - k_2 d_2 \sin(\sigma_{\mathbf{g}}))\right)\right), \end{aligned} \tag{3}$$

In environments with no scattering, where $\sigma_{\mathbf{g}} = 0$, it should be noted that (3) simplifies to

$$[\bar{\mathbf{g}}]_k = \alpha \exp\left(-j\frac{2\pi}{\lambda} r_k \cos(\psi_k)\right) \equiv \exp\left(-j\frac{2\pi d_1}{\lambda}|k_1|\right), \tag{4}$$

where $\alpha = \alpha_1 + \alpha_2$ in (4) with a unitary power is a common multiplicative factor that can be ultimately neglected for simplification without consequences.

A dual-hop communication link is established between the source S and the destination D. During the first time slot, S transmits its signal, s, to the WSAN. Let $\mathbf{y}$ be the signal vector received by the WSAN nodes, represented by

$$\mathbf{y} = \bar{\mathbf{g}} s + \mathbf{v}, \tag{5}$$

where $\bar{\mathbf{g}} \triangleq [[\bar{\mathbf{g}}]_1 \dots [\bar{\mathbf{g}}]_K]^T$ is the nominal backward channel vector, and $\mathbf{v}$ represents the i.i.d. Gaussian noise vector, where each element has the same element-wise variance, $\sigma_{\mathbf{v}}^2$.

During the second time slot, the k-th node applies the complex conjugate of the beamforming weight w_k to its received signal and then transmits the processed signal to the destination D. From (5), the signal received at the destination D is given by

$$\begin{aligned} r &= \bar{\mathbf{f}}^T(\mathbf{w}^* \odot \mathbf{y}) + n \\ &= s\mathbf{w}^H \bar{\mathbf{h}} + \mathbf{w}^H(\bar{\mathbf{f}} \odot \mathbf{v}) + n, \end{aligned} \tag{6}$$

where $\mathbf{w} \triangleq [w_1 \dots w_K]$ represents the beamforming vector, $\bar{\mathbf{h}} \triangleq \bar{\mathbf{f}} \odot \bar{\mathbf{g}}$ is the nominal dual-hop channel vector, and $\bar{\mathbf{f}} \triangleq [[\bar{\mathbf{f}}]_1 \dots [\bar{\mathbf{f}}]_K]^T$ is the nominal forward channel vector. Additionally, n denotes the scalar Gaussian noise received at the destination D with the variance σ_n^2.

Let $\bar{P}_{\mathbf{w},S}$ represent the total received power from the forwarded copies of the source S by the WSAN and $\bar{P}_{\mathbf{w},n}$ denote the total received noise power, which results from the scalar

noise n at the destination D and the noise vector $\mathbf{v}$ transmitted from the WSAN nodes. From (6), we have the following relationship:

$$\bar{P}_{\mathbf{w},S} = \left|\mathbf{w}^H\bar{\mathbf{h}}\right|^2, \tag{7}$$

$$\bar{P}_{\mathbf{w},n} = \sigma_v^2\mathbf{w}^H\bar{\mathbf{\Lambda}}\mathbf{w} + \sigma_n^2, \tag{8}$$

where $\bar{\mathbf{\Lambda}} \triangleq \text{diag}\{|[\bar{\mathbf{f}}]_1|^2 \dots |[\bar{\mathbf{f}}]_K|^2\}$. We propose in this work a solution that aims to minimize the total noise power while ensuring that the beamforming response $\mathbf{w}^H\bar{\mathbf{h}}$ remains unchanged, thereby keeping the power received at the destination D equal to unity. This approach essentially corresponds to the well-known minimum-variance distortionless response (MVDR) beamforming criterion with a relaxed constraint on the distortionless response [33]. Mathematically, this can be formulated as the following constrained optimization problem:

$$\bar{\mathbf{w}} = \arg\max \frac{\mathbf{w}^H\bar{\mathbf{h}}\bar{\mathbf{h}}^H\mathbf{w}}{\mathbf{w}^H\bar{\mathbf{\Lambda}}\mathbf{w}} \quad \text{s.t.} \quad \left|\mathbf{w}^H\bar{\mathbf{h}}\right|^2 = 1. \tag{9}$$

The optimal solution to the convex optimization problem outlined above can be derived as

$$\bar{\mathbf{w}} = \frac{\bar{\mathbf{\Lambda}}^{-1}\bar{\mathbf{h}}}{\left|\bar{\mathbf{h}}^H\bar{\mathbf{\Lambda}}^{-1}\bar{\mathbf{h}}\right|}, \tag{10}$$

and, as a result, the weight of the k-th node is determined by

$$[\bar{\mathbf{w}}]_k = \frac{[\bar{\mathbf{\Lambda}}^{-1}\bar{\mathbf{h}}]_k}{\left|\bar{\mathbf{h}}^H\bar{\mathbf{\Lambda}}^{-1}\bar{\mathbf{h}}\right|}. \tag{11}$$

3. Proposed RDCB Techniques

3.1. Placement-Error-Free Implementation Scenarios

In the ideal scenario when there are no errors related to node placement (i.e., $\sigma_x = \sigma_y = \delta_{k_1} = \delta_{k_2} = 0$), the nominal channel coefficients from (1), (2), (3), and (4) are exactly the same as the actual coefficients. As a result, in dual-hop polychromatic–monochromatic propagation scenarios, the optimal CB solution given in (11) takes the form of $\bar{\mathbf{w}}_{\text{PM}-\text{DCB}}$ in (A1) (see Appendix A). In dual-hop bichromatic–monochromatic and monochromatic–monochromatic propagation scenarios, the optimal CB solution in (11) simplifies to $\bar{\mathbf{w}}_{\text{BM}-\text{DCB}}$ in (A2) and $\bar{\mathbf{w}}_{\text{MM}-\text{DCB}}$ in (A4) (see Appendix A).

It is easy to verify that $\bar{\mathbf{w}}_{\text{PM}-\text{DCB}}$ and $\bar{\mathbf{w}}_{\text{BM}-\text{DCB}}$ reduce to $\bar{\mathbf{w}}_{\text{MM}-\text{DCB}}$ in a scattering-free environment (i.e., when $\sigma_{\mathbf{g}} = 0$). In the subsequent section on simulation results, we will demonstrate that their performances degrade in more realistic scenarios when there are node placement errors unaccounted for in their design, thereby leading to channel mismatch.

3.2. Placement-Error-Prone Implementation Scenarios

In practical scenarios where node placement errors are present, we derive the expressions for the true channel coefficients to replace the nominal ones defined earlier in (1), (2), (3), and (4) as follows, respectively:

$$[\mathbf{g}]_k = \sum_{l=1}^{L} \alpha_l \exp\left(-j\left(\frac{2\pi}{\lambda}(|k_1|d_1\cos(\phi_l) + k_2 d_2 \sin(\phi_l))\right)\right) \times \exp\left(-j\left(\frac{2\pi}{\lambda}(\delta_{k_1} d_1\cos(\phi_l) + \delta_{k_2} d_2 \sin(\phi_l))\right)\right), \tag{12}$$

$$\begin{aligned}[\mathbf{f}]_k &= \exp\left(-j\left(\frac{2\pi}{\lambda}(|k_1|d_1\cos(\phi_D)+k_2d_2\sin(\phi_D))\right)\right)\\ &\times \exp\left(-j\frac{2\pi}{\lambda}(d_1\cos(\phi_D)\delta_{k_1}+d_2\sin(\phi_D)\delta_{k_2})\right)\\ &= [\bar{\mathbf{f}}]_k\delta_{\mathbf{f}_k},\end{aligned} \tag{13}$$

$$\begin{aligned}[\mathbf{g}]_k &= \alpha_1\exp\left(-j\left(\frac{2\pi}{\lambda}(|k_1|d_1\cos(\sigma_\mathbf{g})+k_2d_2\sin(\sigma_\mathbf{g}))\right)\right)\\ &\times \exp\left(-j\left(\frac{2\pi}{\lambda}(\delta_{k_1}d_1\cos(\sigma_\mathbf{g})+\delta_{k_2}d_2\sin(\sigma_\mathbf{g}))\right)\right)\\ &+ \alpha_2\exp\left(-j\left(\frac{2\pi}{\lambda}(|k_1|d_1\cos(\sigma_\mathbf{g})-k_2d_2\sin(\sigma_\mathbf{g}))\right)\right)\\ &\times \exp\left(-j\left(\frac{2\pi}{\lambda}(\delta_{k_1}d_1\cos(\sigma_\mathbf{g})-\delta_{k_2}d_2\sin(\sigma_\mathbf{g}))\right)\right),\end{aligned} \tag{14}$$

and

$$\begin{aligned}[\mathbf{g}]_k &= \exp\left(-j\frac{2\pi d_1}{\lambda}|k_1|\right)\exp\left(-j\frac{2\pi d_1}{\lambda}\delta_{k_1}\right)\\ &= [\bar{\mathbf{g}}]_k\delta_{\mathbf{g}_k}.\end{aligned} \tag{15}$$

If, in an ideal scenario, the WSAN had perfect knowledge of the true channel coefficients with their placement errors relative to their nominal positions, the constrained optimization problem in (9) and its corresponding optimal solution in (11) would be reformulated as

$$\breve{\mathbf{w}} = \arg\max \frac{\mathbf{w}^H\mathbf{h}\mathbf{h}^H\mathbf{w}}{\mathbf{w}^H\mathbf{\Lambda}\mathbf{w}} \quad \text{s.t.} \quad \left|\mathbf{w}^H\mathbf{h}\right|^2 = 1, \tag{16}$$

and

$$\breve{\mathbf{w}} = \frac{\mathbf{\Lambda}^{-1}\mathbf{h}}{|\mathbf{h}^H\mathbf{\Lambda}^{-1}\mathbf{h}|}, \tag{17}$$

thereby resulting in the "genie-type" beamformer $\breve{\mathbf{w}}_{\mathrm{PM-DCB}}$, $\breve{\mathbf{w}}_{\mathrm{BM-DCB}}$, or $\breve{\mathbf{w}}_{\mathrm{MM-DCB}}$ when plugging into (17) the expression for the true forward channel coefficients in (13) and one of the three expressions for the true backward channel coefficients in (12), (14), or (15), respectively. However, $\breve{\mathbf{w}}_{\mathrm{PM-DCB}}$, $\breve{\mathbf{w}}_{\mathrm{BM-DCB}}$, and $\breve{\mathbf{w}}_{\mathrm{MM-DCB}}$ cannot be practically implemented as the WSAN is unaware of the precise expressions for the location-error-sensitive backward and forward channels $\mathbf{g}$ and $\mathbf{f}$, respectively.

In the following, we introduce new RDCB approaches that are robust to node placement errors in scattered environments. Our approach leverages the following: (i) highly efficient asymptotic approximations for large numbers, K, of WSAN nodes, (ii) the inherent geometric symmetries of the deterministic rectangular grid layout, and (iii) prior information about the variances σ_x^2 and σ_y^2, which describe the second-order statistics of the placement errors with respect to their nominal positions. By performing so, we derive new solutions in closed form that account for the inevitable phase jitter caused by node placement errors and, hence, incorporate their impact into the CB design. This is accomplished by loosening the optimization criterion in (16) to incorporate all possible placement error scenarios through averaging both the numerator and denominator while keeping the relaxed distortionless response constraint intact:

$$\mathbf{w} = \arg\max \frac{\mathbb{E}_{\delta_{k_1},\delta_{k_2}}[\mathbf{w}^H\mathbf{h}\mathbf{h}^H\mathbf{w}]}{\mathbb{E}_{\delta_{k_1},\delta_{k_2}}[\mathbf{w}^H\mathbf{\Lambda}\mathbf{w}]} \quad \text{s.t.} \quad \left|\mathbf{w}^H\mathbf{h}\right|^2 = 1. \tag{18}$$

It can be demonstrated that the optimization problem in (18) simplifies to a combined version of (9) and (16):

$$\mathbf{w} = \arg\max \frac{\mathbf{w}^H \bar{\mathbf{h}} \bar{\mathbf{h}}^H \mathbf{w}}{\mathbf{w}^H \bar{\mathbf{\Lambda}} \mathbf{w}} \quad \text{s.t.} \quad \left|\mathbf{w}^H \mathbf{h}\right|^2 = 1. \tag{19}$$

The resulting optimal robust beamforming vector is expressed as

$$\mathbf{w}_{\text{RDCB}} = \frac{\bar{\mathbf{\Lambda}}^{-1} \bar{\mathbf{h}}}{\left|\bar{\mathbf{h}}^H \bar{\mathbf{\Lambda}}^{-1} \mathbf{h}\right|}. \tag{20}$$

We observe from (20) that $\mathbf{w}_{\text{RDCB}}$ involves both the true and nominal channel values. However, since the nodes are unaware of the true channel, it is necessary to replace $\left|\bar{\mathbf{h}}^H \bar{\mathbf{\Lambda}}^{-1} \mathbf{h}\right|$ with an equivalent approximation, $\Xi_{\star M}$, with $\star \in \{P, B, M\}$ for the poly-, bi-, and monochromatic cases, respectively, that relies only on parameters available at each node of the WSAN, i.e., for $\star \in \{P, B, M\}$ we have:

$$\mathbf{w}_{\star\text{M}-\text{RDCB}} = \frac{\bar{\mathbf{\Lambda}}^{-1} \bar{\mathbf{h}}}{\Xi_{\star M}}. \tag{21}$$

To achieve this, we define the comprehensive substitute $\Xi_{\star M}$ as the asymptotic expression of $\left|\bar{\mathbf{h}}^H \bar{\mathbf{\Lambda}}^{-1} \mathbf{h}\right|$ derived and validated through numerical methods at reasonably large values of K. Specifically, by applying the law of large numbers, one can demonstrate the expressions of $\Xi_{\star\text{M}}$ with $\star \in \{\text{P}, \text{B}, \text{M}\}$ in (A5)–(A7) (see Appendix B) for large values of K in dual-hop polychromatic–monochromatic, bichromatic–monochromatic, and monochromatic–monochromatic propagation scenarios, respectively.

Since WSANs usually consist of a large number of nodes, we can replace (A5), (A6), or (A7) in (21) to derive $\mathbf{w}_{\text{PM}-\text{RDCB}}$, $\mathbf{w}_{\text{BM}-\text{RDCB}}$, or $\mathbf{w}_{\text{MM}-\text{RDCB}}$, respectively.

Thus, it can be concluded that $\mathbf{w}_{\text{PM}-\text{RDCB}}$, $\mathbf{w}_{\text{BM}-\text{RDCB}}$, and $\mathbf{w}_{\text{MM}-\text{RDCB}}$ rely exclusively on locally available information at each node, specifically $[\bar{\mathbf{h}}]_k$, σ_x, and σ_y. The first is reconstructed directly at the k-th node, while σ_x and σ_y can be broadcast across the WSAN with minimal overhead, computational cost, and power consumption. This inherent feature of DCB eliminates the need for inter-node communication, thus saving energy resources and improving the overall spectral efficiency of the WSAN. It is also noteworthy that when there is no scattering over the first hop, $\mathbf{w}_{\text{PM}-\text{RDCB}}$ and $\mathbf{w}_{\text{BM}-\text{RDCB}}$ reduce to $\mathbf{w}_{\text{MM}-\text{RDCB}}$, and that $\mathbf{w}_{\text{PM}-\text{RDCB}}$, $\mathbf{w}_{\text{BM}-\text{RDCB}}$, and $\mathbf{w}_{\text{MM}-\text{RDCB}}$ further simplify to $\breve{\mathbf{w}}_{\text{PM}-\text{DCB}} = \bar{\mathbf{w}}_{\text{PM}-\text{DCB}}$, $\breve{\mathbf{w}}_{\text{BM}-\text{DCB}} = \bar{\mathbf{w}}_{\text{BM}-\text{DCB}}$, and $\breve{\mathbf{w}}_{\text{MM}-\text{DCB}} = \bar{\mathbf{w}}_{\text{MM}-\text{DCB}}$, respectively, when there are no placement errors among the nodes.

4. Numerical Evaluation Results

This section presents a numerical evaluation of the performance improvements achieved by the proposed RDCB solutions against the nominal optimal CB approaches $\bar{\mathbf{w}}_{\text{MM}-\text{opt}}$, $\bar{\mathbf{w}}_{\text{BM}-\text{opt}}$, and $\bar{\mathbf{w}}_{\text{PM}-\text{opt}}$ derived from (10). The simulation setup parameters are specified in Table 2 where, unless specified otherwise, we consider by default $K_1 = K_2 = K_0 = \sqrt{K}$ for $K = 64, 256, 1024,$ and 4096; $d_1 = d_2 = d = \lambda/2$ when d is fixed; both σ_n^2 and σ_v^2 set to 10 dB below the source transmit power; and $\phi_D \approx 17$ degrees.

We chose the average-signal-to-average-noise ratio (ASANR) as our performance metric over the average signal-to-noise ratio (ASNR), primarily because the derivation of the ASNR is notably intricate. The ASANR provides a practical and efficient alternative, particularly for very large K, as previously validated in [5]. We conducted Monte Carlo simulations with averages computed over $M_c = 10^5$ independent random realizations.

Figure 2 illustrates both nominal and true WSAN grid positions with $K_1 = K_2 = 8$ ($K = 64$) and $\sigma_x = \sigma_y$ set to 0.1 or 0.25 in sub-plots (a) and (b), respectively. It indicates that

the grid becomes significantly distorted at 0.1. Yet, we consider values as high as 0.25 and even beyond where the grid basically loses its deterministic geometric structure. In the following, we assess the impact of multiple parameters while accounting for varying levels of placement errors.

Table 2. Simulation setup parameters.

Variable		Notation	Value (s)
Total number of grid nodes		K	64, 256, 1024, 4096
Grid nodes over x and y	Square	$K_1 = K_2$	$\sqrt{K}$
	Rectangle	$K_i = 4K_j$ $i \neq j$ $i, j \in \{1, 2\}$	$2\sqrt{K}$, $\sqrt{K}/2$
Inter-node distances over x and y		$d_1 = d_2 = d$	$\lambda/2$ when fixed or [0.1:0.1:0.8] λ
AoA at D		ϕ_D	17 degrees
AoD at S		ϕ_S	0 degrees
AS around AoD of S	Low	σ_g	0 degrees
	Moderate		6 degrees
	High		60 degrees
AS around AoA of D		σ_f	0 degrees
Approximate number of polychromatic rays in high scattering		L	10
Rx noise power at nodes below Tx power of S		σ_n^2	10 dB when fixed or [0, 10, 20] dB
Rx noise power at D below Tx power of S		σ_v^2	10 dB when fixed or [0, 10, 20] dB
Normalized standard deviation of nodes placement errors		$\sigma_x = \sigma_y$	0:0.02:0.26 or specified
Monte Carlo realizations		M_c	10^5

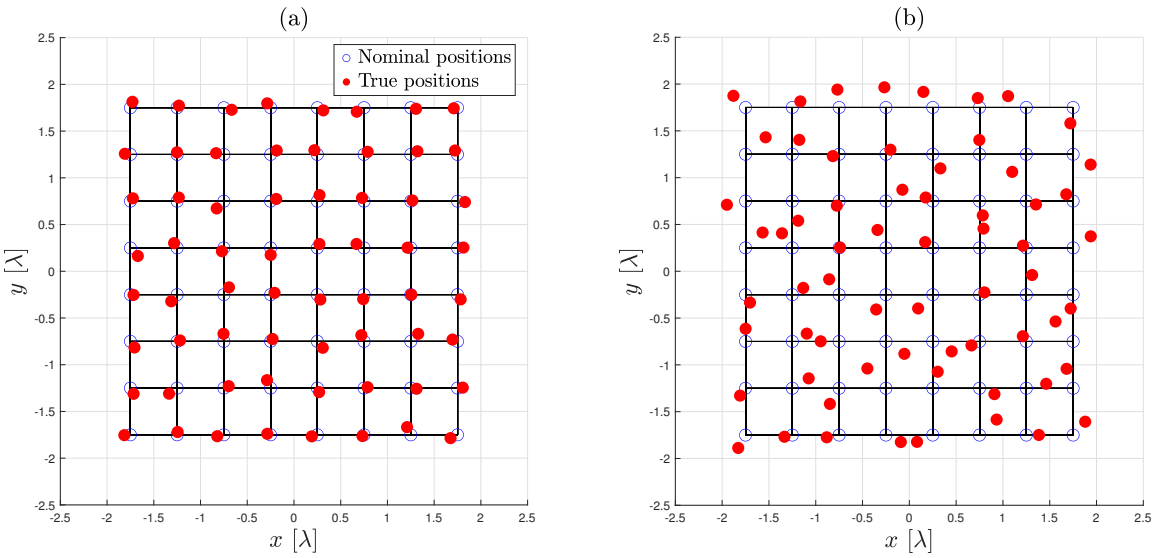

Figure 2. Illustrations of the nominal (blue circles) and true (red dots) square-grid positions for a WSAN of $K = 64$ nodes (i.e., $K_1 = K_2 = 8$) with (**a**) $\sigma_x = \sigma_y = 0.1$ and (**b**) $\sigma_x = \sigma_y = 0.25$.

In Table 3, the ASANR values corresponding to $\mathbf{w}_{\mathrm{PM-RDCB}}$ are reported for dual-hop polychromatic–monochromatic configurations. These results consider three distinct values of ϕ_D, representing the AoA at the destination D, with parameters set as $K = 4096$; $d/\lambda = 0.5$; $\sigma_g = 60$ degrees; and $\sigma_x = \sigma_y = 0.1$. Regardless of the angle (whether extreme fire-end or broadside), the ASANR remains consistently close to optimal at around 10 dB; this outcome confirms (i) the accuracy of the analytical calculations, independent of the chosen ϕ_D values, and (ii) the soundness of assuming the AoD at the source S to be $\phi_S = 0$, without any loss of generality or impact on the results.

Table 3. ASANR performance of proposed $\mathbf{w}_{\mathrm{PM-RDCB}}$ with different AoA ϕ_D values at destination D in dual-hop polychromatic–monochromatic scenarios (i.e., $\sigma_g = 60$ degrees) with $K = 4096$; $d/\lambda = 0.5$; and $\sigma_x = \sigma_y = 0.1$.

AoA ϕ_D at destination D	$-\pi/2$	π	$\pi/2$
ASANR (dB)	10.0169	10.0149	10.0151

Figures 3–5 plot the performance of the proposed $\mathbf{w}_{\mathrm{MM-RDCB}}$ in terms of the analytical ASANR, numerical ASNR, and analytical ASANR gains against the nominal $\bar{\mathbf{w}}_{\mathrm{MM-DCB}}$ versus $\sigma_x = \sigma_y$ for various values of $K_1 > K_2$ (For the sake of conciseness, we did not include in this article similar results obtained in the case of $K_2 < K_1$ (i.e., landscape-oriented rectangular grids).). The results indicate that as K increases, both the ASANR and ASNR improve until they reach their optimal values. Additionally, the analytical ASANR and numerical ASNR align perfectly, corroborating the appropriateness of our selected performance metric. We further observe that both square and rectangular WSAN layouts lead to the same observations. The plots also reveal significant ASANR gains of up to 18 dB across the evaluated range of $\sigma_x = \sigma_y$. Specifically, we reach an ASANR gain up to 1.7 dB and 15.6 dB for $\sigma_x = \sigma_y = 0.1$ and 0.25, respectively. These results, coupled with earlier findings, reinforce the efficiency and robustness of $\mathbf{w}_{\mathrm{MM-RDCB}}$ against node placement errors and further verify our theoretical models.

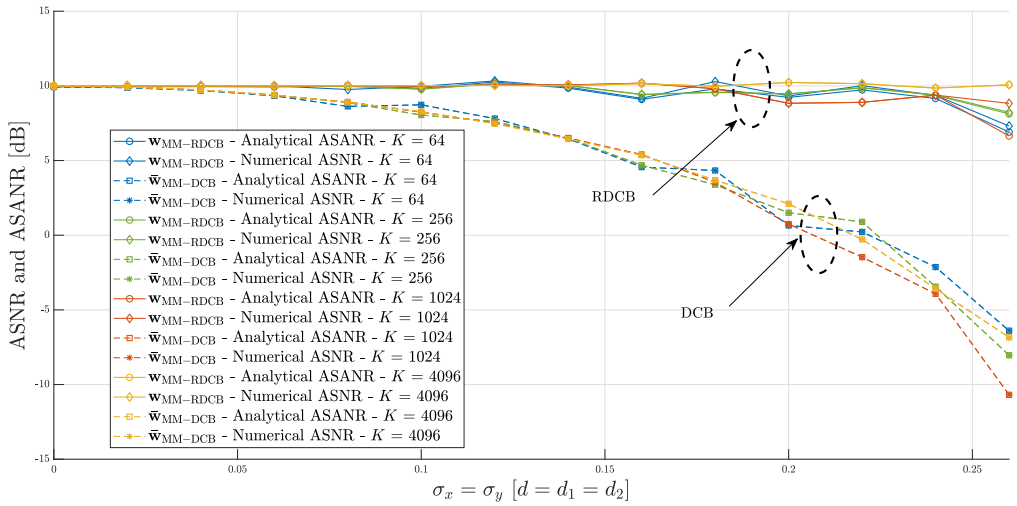

Figure 3. Performance evaluation of the proposed $\mathbf{w}_{\mathrm{MM-RDCB}}$ in terms of the numerical ASNR and analytical ASANR and the nominal $\bar{\mathbf{w}}_{\mathrm{MM-DCB}}$ in terms of the numerical ASANR vs. the normalized standard deviation of node placement errors in dual-hop monochromatic–monochromatic scenarios (i.e., $\sigma_g = 0$ degrees) [9] over a square grid of $K = 64, 256, 1024, 4096$ nodes with $K_1 = K_2 = \sqrt{K}$ and $d/\lambda = 0.5$.

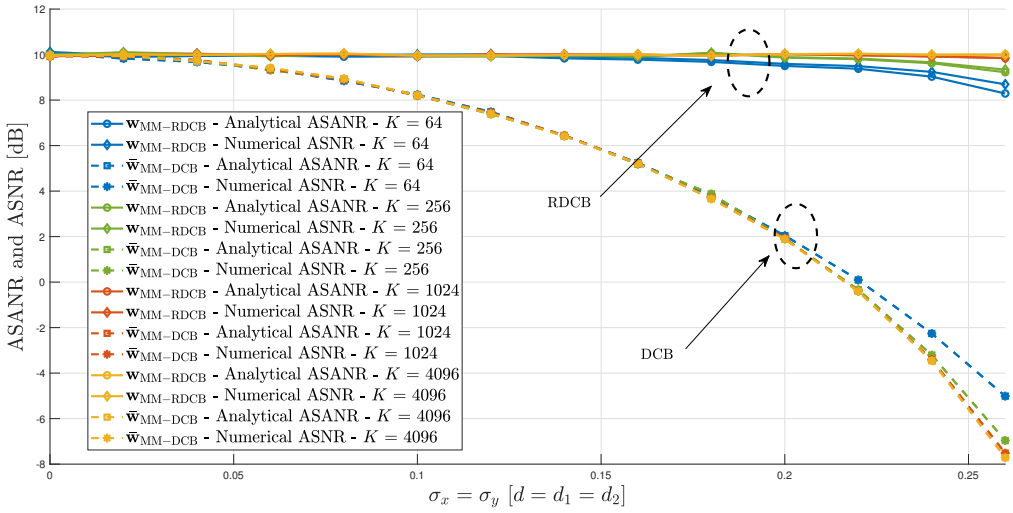

Figure 4. Performance evaluation of the proposed $\mathbf{w}_{\mathrm{MM-RDCB}}$ in terms of the numerical ASNR and analytical ASANR and the nominal $\bar{\mathbf{w}}_{\mathrm{MM-DCB}}$ in terms of the numerical ASANR vs. the normalized standard deviation of node placement errors in dual-hop monochromatic–monochromatic scenarios (i.e., $\sigma_g = 0$ degrees) [9] over a portrait-oriented rectangular grid of $K = 64, 256, 1024, 4096$ nodes with $K_1 = \sqrt{K}/2 < K_2 = 2\sqrt{K}$ and $d/\lambda = 0.5$.

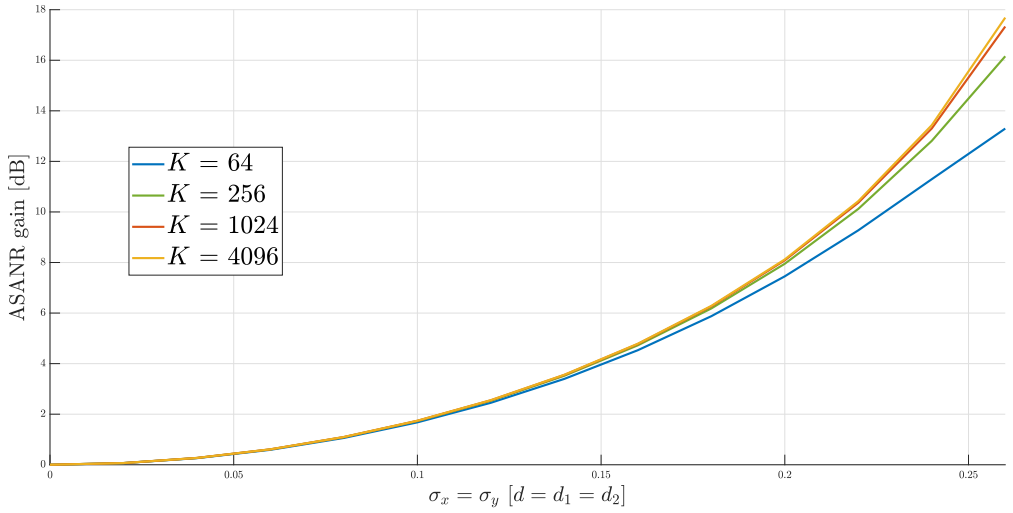

Figure 5. Performance evaluation of the proposed $\mathbf{w}_{\mathrm{MM-RDCB}}$ in terms of the ASANR gain against the nominal $\bar{\mathbf{w}}_{\mathrm{MM-DCB}}$ vs. the normalized standard deviation of node placement errors in dual-hop monochromatic–monochromatic scenarios (i.e., $\sigma_g = 0$ degrees) [9] for $K = 64, 256, 1024, 4096$ and $d/\lambda = 0.5$.

Figures 6–8 display the performance of the proposed $\mathbf{w}_{\mathrm{BM-RDCB}}$ in terms of the analytical ASANR, numerical ASNR, and analytical ASANR gains against the nominal $\bar{\mathbf{w}}_{\mathrm{BM-DCB}}$ versus $\sigma_x = \sigma_y$ for various values of K. Given the slight to moderate scattering present in the S-WSAN communication link, higher values of K are needed for the ASANR to reach optimal performance and ensure its alignment with the ASNR. This trend can be attributed to the fact that larger node arrays allow for more precise spatial beamforming, effectively mitigating the detrimental effects of node placement errors. At lower values of K, the degradation in the ASANR highlights the sensitivity of $\bar{\mathbf{w}}_{\mathrm{BM-DCB}}$ to spatial errors, emphasizing the need for tighter node placement control in practical implementations. This is mainly due to the law of large numbers used to calculate the beamforming weights.

Assuming large values for K is a valid hypothesis when considering the massive connectivity typical of new 5G and future 5G+/6G wireless technologies as well as of the IoT. Specifically, Figure 6 shows that $K = 256$ or higher can achieve nearly optimal performance. The plots also reveal significant ASANR gains of up to 17 dB across the evaluated range of $\sigma_x = \sigma_y$. Specifically, we reach an ASANR gain of up to 2 dB and 15 dB for $\sigma_x = \sigma_y = 0.1$ and 0.25, respectively. It is worth noting from Figure 7 that the ASANR gain reaches up to 14 dB when $K_2 = 4K_1$.

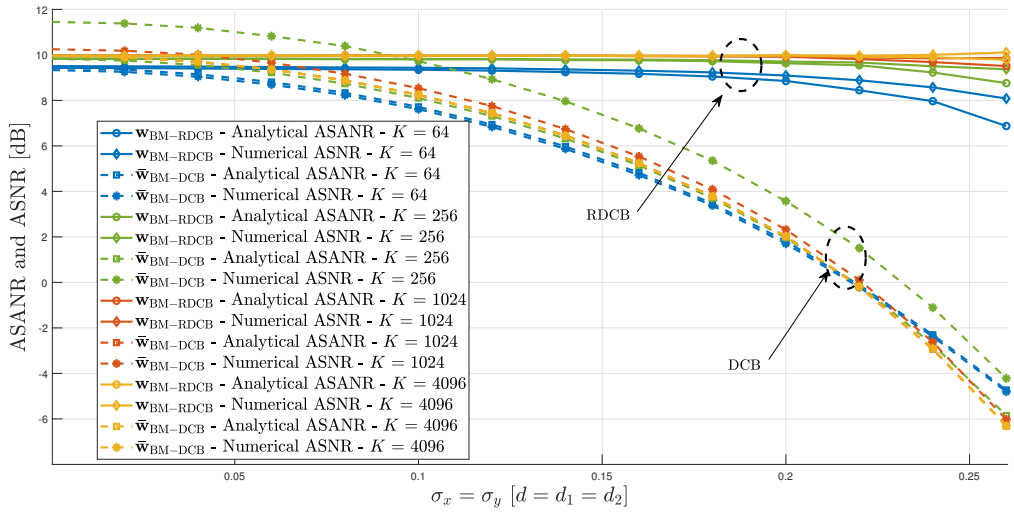

Figure 6. Performance evaluation of the proposed $\mathbf{w}_{\mathrm{BM-RDCB}}$ in terms of the numerical ASNR and analytical ASANR and the nominal $\bar{\mathbf{w}}_{\mathrm{BM-DCB}}$ in terms of the numerical ASANR vs. the normalized standard deviation of node placement errors in dual-hop bichromatic–monochromatic scenarios (i.e., $\sigma_g = 6$ degrees) over a square grid of $K = 64, 256, 1024, 4096$ nodes with $K_1 = K_2 = \sqrt{K}$ and $d/\lambda = 0.5$.

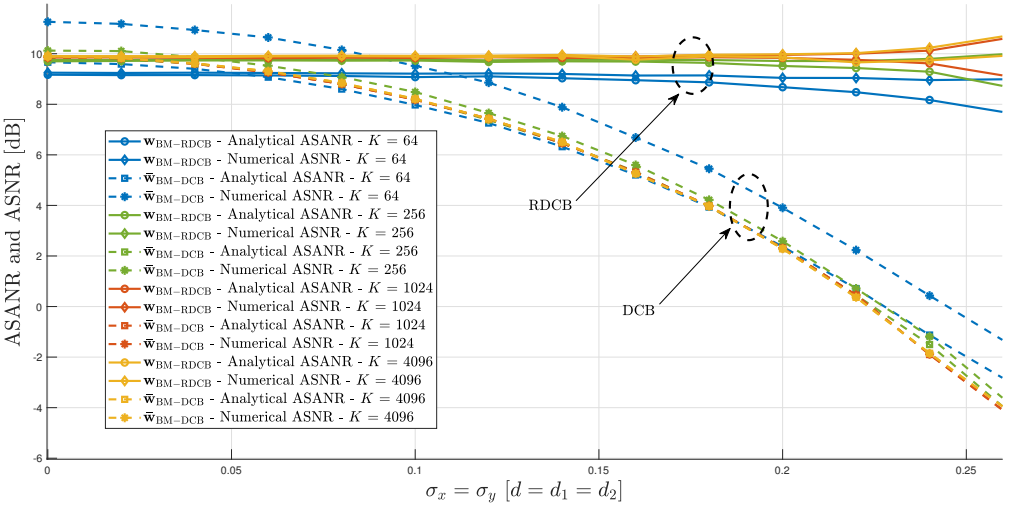

Figure 7. Performance evaluation of the proposed $\mathbf{w}_{\mathrm{BM-RDCB}}$ in terms of the numerical ASNR and analytical ASANR and the nominal $\bar{\mathbf{w}}_{\mathrm{BM-DCB}}$ in terms of the numerical ASANR vs. the normalized standard deviation of node placement errors in dual-hop bichromatic–monochromatic scenarios (i.e., $\sigma_g = 6$ degrees) over a portrait-oriented rectangular grid of $K = 64, 256, 1024, 4096$ nodes with $K_1 = \sqrt{K}/2 < K_2 = 2\sqrt{K}$ and $d/\lambda = 0.5$.

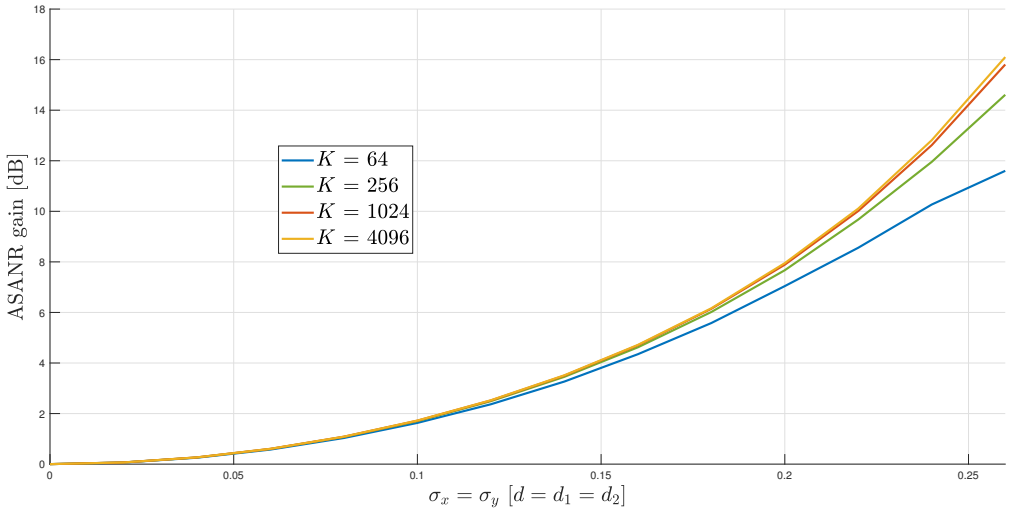

Figure 8. Performance evaluation of the proposed $\mathbf{w}_{\mathrm{BM-RDCB}}$ in terms of the ASANR gain against the nominal $\bar{\mathbf{w}}_{\mathrm{BM-DCB}}$ vs. the normalized standard deviation of node placement errors in dual-hop bichromatic–monochromatic scenarios (i.e., $\sigma_g = 6$ degrees) for $K = 64, 256, 1024, 4096$ and $d/\lambda = 0.5$.

Figures 9–11 plot the performance of the proposed $\mathbf{w}_{\mathrm{PM-RDCB}}$ in terms of the analytical ASANR, numerical ASNR, and analytical ASANR gains against the nominal $\bar{\mathbf{w}}_{\mathrm{PM-DCB}}$ versus $\sigma_x = \sigma_y$ for various values of K. Figure 11 shows that even relatively low K values can achieve nearly optimal performance for the three tested WSAN layouts. The plots also reveal significant ASANR gains of up to 10 dB across the evaluated range of $\sigma_x = \sigma_y$. Specifically, we reach an ASANR gain of up to 1.5 dB and 9.2 dB for $\sigma_x = \sigma_y = 0.1$ and 0.25, respectively. This difference with $\bar{\mathbf{w}}_{\mathrm{BM-DCB}}$ suggests that while $\bar{\mathbf{w}}_{\mathrm{PM-DCB}}$ maintains stability under varying conditions, it does not achieve the same peak performance as $\bar{\mathbf{w}}_{\mathrm{BM-DCB}}$ in the absence of severe placement errors. This trade-off highlights the need to balance robustness and gain efficiency when choosing between different RDCB techniques for practical applications.

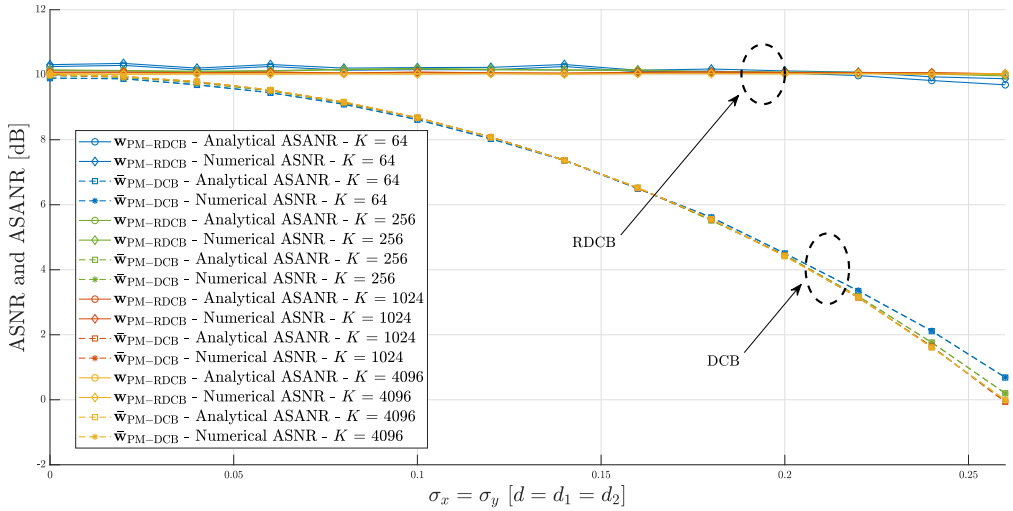

Figure 9. Performance evaluation of the proposed $\mathbf{w}_{\mathrm{PM-RDCB}}$ in terms of the numerical ASNR and analytical ASANR and the nominal $\bar{\mathbf{w}}_{\mathrm{PM-DCB}}$ in terms of the numerical ASANR vs. the normalized standard deviation of node placement errors in dual-hop polychromatic–monochromatic scenarios (i.e., $\sigma_g = 60$ degrees) over a square grid of $K = 64, 256, 1024, 4096$ nodes with $K_1 = K_2 = \sqrt{K}$ and $d/\lambda = 0.5$.

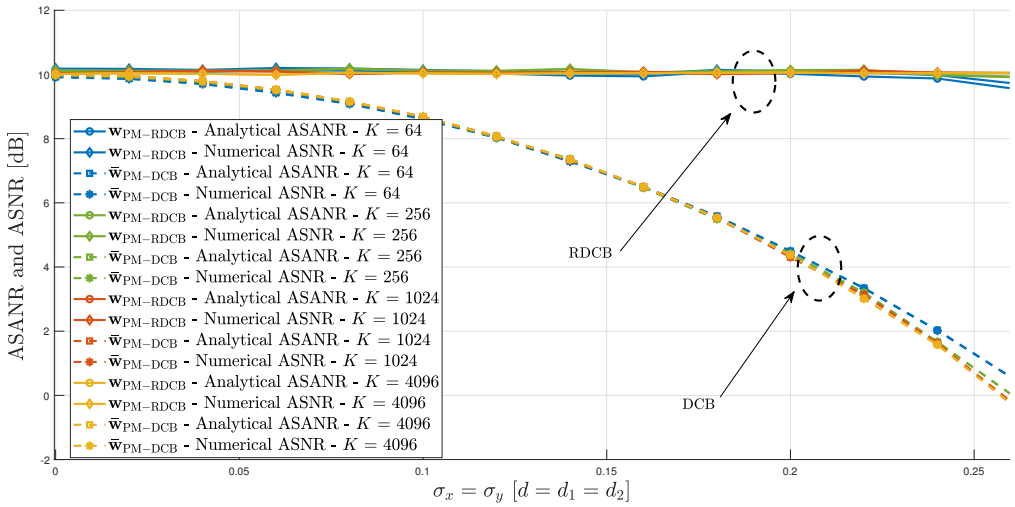

Figure 10. Performance evaluation of the proposed $\mathbf{w}_{\mathrm{PM-RDCB}}$ in terms of the numerical ASNR and analytical ASANR and the nominal $\bar{\mathbf{w}}_{\mathrm{PM-DCB}}$ in terms of the numerical ASANR vs. the normalized standard deviation of node placement errors in dual-hop polychromatic–monochromatic scenarios (i.e., $\sigma_g = 60$ degrees) over a portrait-oriented rectangular grid of $K = 64, 256, 1024, 4096$ nodes with $K_1 = \sqrt{K}/2 < K_2 = 2\sqrt{K}$ and $d/\lambda = 0.5$.

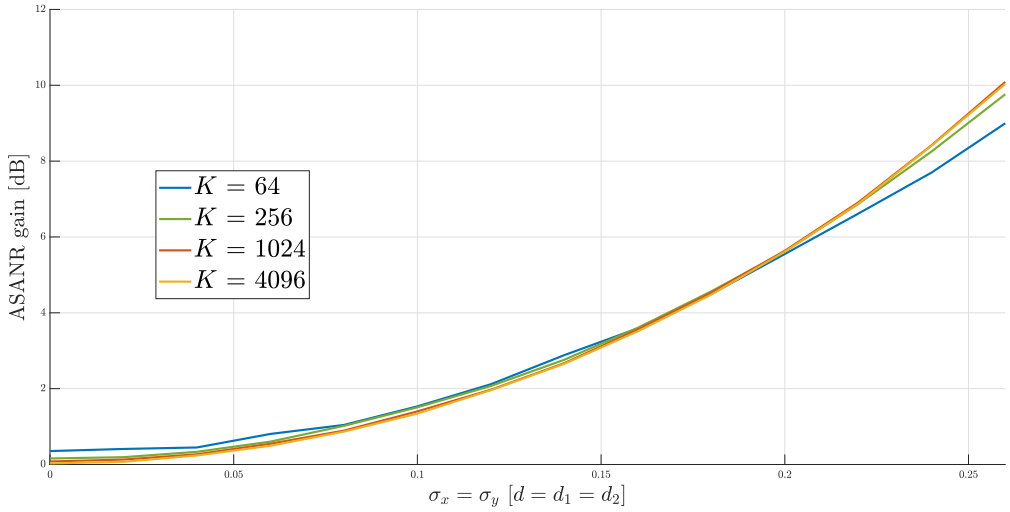

Figure 11. Performance evaluation of the proposed $\mathbf{w}_{\mathrm{PM-RDCB}}$ in terms of the ASANR gain against the nominal $\bar{\mathbf{w}}_{\mathrm{PM-DCB}}$ vs. the normalized standard deviation of node placement errors in dual-hop polychromatic–monochromatic scenarios (i.e., $\sigma_g = 60$ degrees) for $K = 64, 256, 1024, 4096$ and $d/\lambda = 0.5$.

Moreover, the analytical ASANR and numerical ASNR align perfectly, corroborating the appropriateness of our selected performance metric. This observation further reinforces the soundness of our mathematical assumptions, while also highlighting the robustness of the proposed RDCB solutions.

Figures 12 and 13 investigate how the ratio of d/λ affects the analytical ASANR, numerical ASNR, and analytical ASANR gains of the proposed $\mathbf{w}_{\mathrm{PM-RDCB}}$ versus the nominal $\bar{\mathbf{w}}_{\mathrm{PM-DCB}}$ against $\sigma_x = \sigma_y$ for $K = 1024$ (Similar results were obtained in the less adverse and challenging mono- and bichromatic cases, indicating the same trends and observations, which are not included here for the sake of conciseness). The results indicate that $\mathbf{w}_{\mathrm{PM-RDCB}}$ reaches near-optimal SNR performance at 10 dB (see Figure 12) for all tested d/λ values, even those that deviate from the standard half-wavelength spacing of

0.5. Additionally, the gains over $\bar{\mathbf{w}}_{\mathrm{PM-DCB}}$ increase with larger d/λ values, reaching up to 21 dB at 0.8 (see Figure 13). Specifically, we reach an ASANR gain up to 3.5 dB and 20.5 dB for $\sigma_x = \sigma_y = 0.1$ and 0.25, respectively. This trend underscores a key trade-off: while increasing d/λ improves the ASANR, practical deployments must consider hardware constraints and synchronization requirements that may limit the feasibility of large node separations.

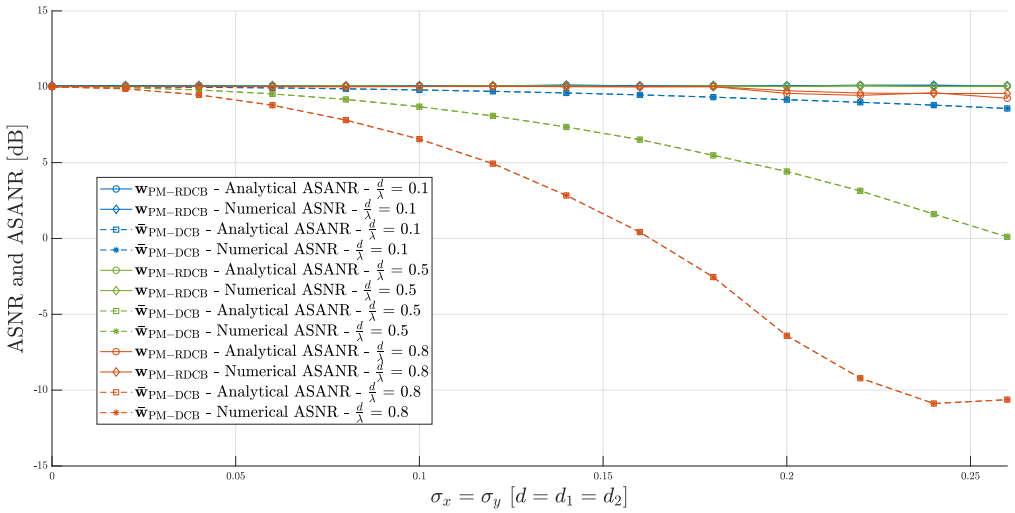

Figure 12. Performance evaluation of the proposed $\mathbf{w}_{\mathrm{PM-RDCB}}$ in terms of the numerical ASNR and analytical ASANR and the nominal $\bar{\mathbf{w}}_{\mathrm{PM-DCB}}$ in terms of the numerical ASANR of vs. the normalized standard deviation of node placement errors in dual-hop polychromatic–monochromatic scenarios (i.e., $\sigma_g = 60$ degrees) for $K = 1024$ and d/λ = 0.1, 0.5, 0.8.

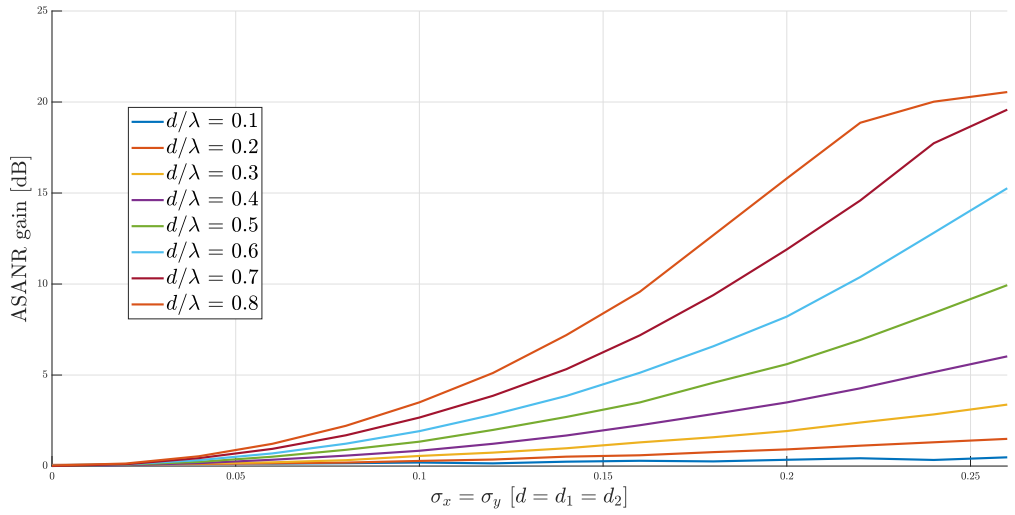

Figure 13. Performance evaluation of the proposed $\mathbf{w}_{\mathrm{PM-RDCB}}$ in terms of the ASANR gain against the nominal $\bar{\mathbf{w}}_{\mathrm{PM-DCB}}$ vs. the normalized standard deviation of node placement errors in dual-hop polychromatic–monochromatic scenarios (i.e., $\sigma_g = 60$ degrees) for $K = 1024$ and d/λ = [0.1:0.1:0.8].

Figures 14–16 examine the impact of the Rx noise power at both the destination D and WSAN nodes. All three results confirm the consistent behavior of $\mathbf{w}_{\mathrm{MM-RDCB}}$, $\mathbf{w}_{\mathrm{BM-RDCB}}$, and $\mathbf{w}_{\mathrm{PM-RDCB}}$ across the three tested noise levels. The three techniques demonstrate robustness against σ_x and σ_y, validating their resilience in different noisy environments.

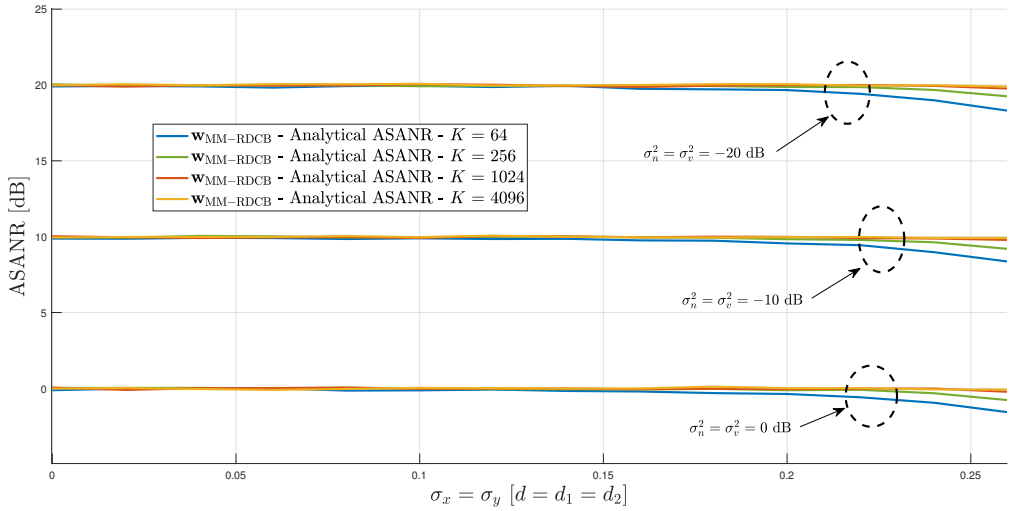

Figure 14. Performance evaluation of the proposed $\mathbf{w}_{\mathrm{MM-RDCB}}$ in terms of the analytical ASANR vs. the normalized standard deviation of node placement errors in dual-hop monochromatic–monochromatic scenarios (i.e., $\sigma_g = 0$ degrees) for $K = 64, 256, 1024, 4096$; $d/\lambda = 0.5$; and $\sigma_n^2 = \sigma_v^2 = [0, -10, -20]$ dB.

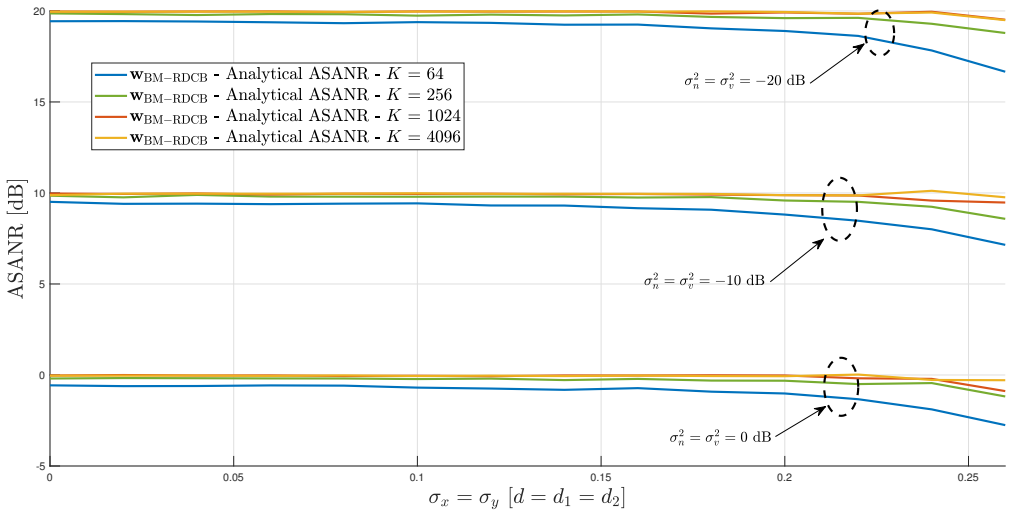

Figure 15. Performance evaluation of the proposed $\mathbf{w}_{\mathrm{BM-RDCB}}$ in terms of the analytical ASANR vs. the normalized standard deviation of node placement errors in dual-hop bichromatic–monochromatic scenarios (i.e., $\sigma_g = 6$ degrees) for $K = 64, 256, 1024, 4096$; $d/\lambda = 0.5$; and $\sigma_n^2 = \sigma_v^2 = [0, -10, -20]$ dB.

Figures 17–19 analyze the performance of $\mathbf{w}_{\mathrm{MM-RDCB}}$, $\mathbf{w}_{\mathrm{BM-RDCB}}$, and $\mathbf{w}_{\mathrm{PM-RDCB}}$, respectively, as a function of the angular spread σ_g. Figure 19 shows that the ASANR performance of $\mathbf{w}_{\mathrm{PM-RDCB}}$ loses only a fraction of the SNR for $K = 256$ and reaches optimal performance for higher K across all tested σ_g values, validating the robustness of the polychromatic technique. On the other hand, Figure 18 shows that $\mathbf{w}_{\mathrm{BM-RDCB}}$ underperforms at very high σ_g values (starting from 20 degrees) for high values of K, as the approximation is designed for low to moderate AS values, and also struggles at very low AS values for only K as low as 64. For K higher than 256, the approximation holds and is robust to node placement errors. Figure 17 shows that for $\sigma_g \leq 0.7$ degrees, $\mathbf{w}_{\mathrm{MM-RDCB}}$ can achieve quasi-optimal performance for K as low as 256, making the monochromatic approximation suitable over this very small range of the angular spread. Additionally, $\mathbf{w}_{\mathrm{BM-RDCB}}$ achieves quasi-optimal performance for $\sigma_g \geq 0.7$ degrees and $\sigma_g \leq 20$ degrees,

where the bichromatic approximation outperforms $\mathbf{w}_{\mathrm{MM-RDCB}}$, which fails to perform well unless σ_g and K are small. In conclusion, the analysis confirms the robustness of the polychromatic approach, achieving near-optimal ASANR performance across all tested σ_g values with minimal SNR loss. The bichromatic approximation performs well for moderate σ_g but struggles at high values, while the monochromatic approach excels for small σ_g. Each technique is effective within its validity range, offering a good trade-off between performance and complexity.

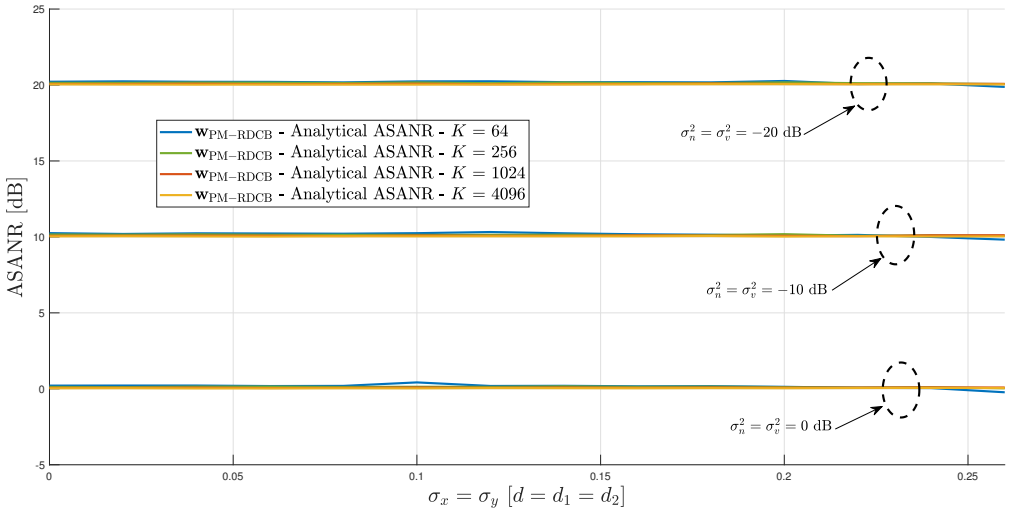

Figure 16. Performance evaluation of the proposed $\mathbf{w}_{\mathrm{PM-RDCB}}$ in terms of the analytical ASANR vs. the normalized standard deviation of node placement errors in dual-hop polychromatic–monochromatic scenarios (i.e., $\sigma_g = 60$ degrees) for $K = 64, 256, 1024, 4096$; $d/\lambda = 0.5$; and $\sigma_n^2 = \sigma_v^2 = [0, -10, -20]$ dB.

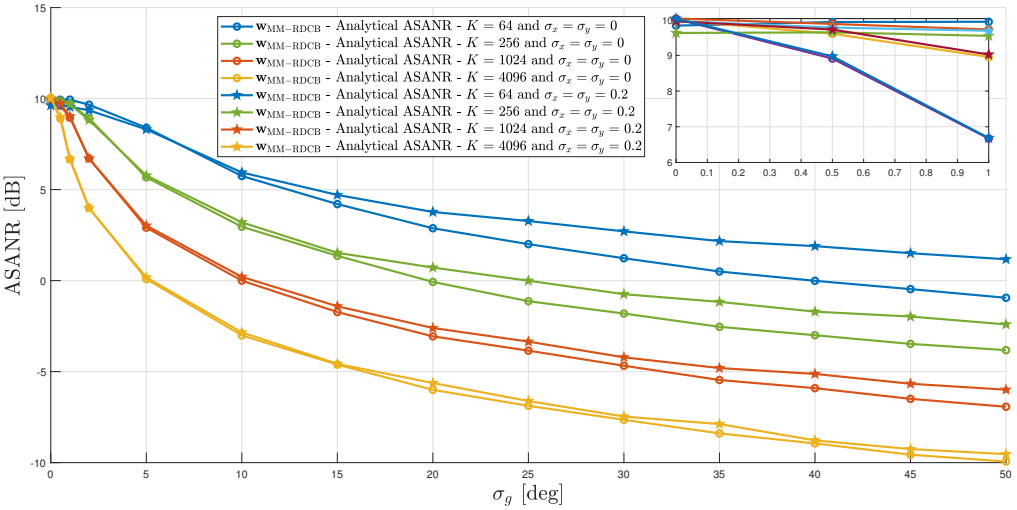

Figure 17. Performance evaluation of the proposed $\mathbf{w}_{\mathrm{MM-RDCB}}$ in terms of the analytical ASANR vs. the angular spread in dual-hop monochromatic–monochromatic scenarios for $K = 64, 256, 1024, 4096$; $d/\lambda = 0.5$; and $\sigma_x = \sigma_y = 0, 0.2$.

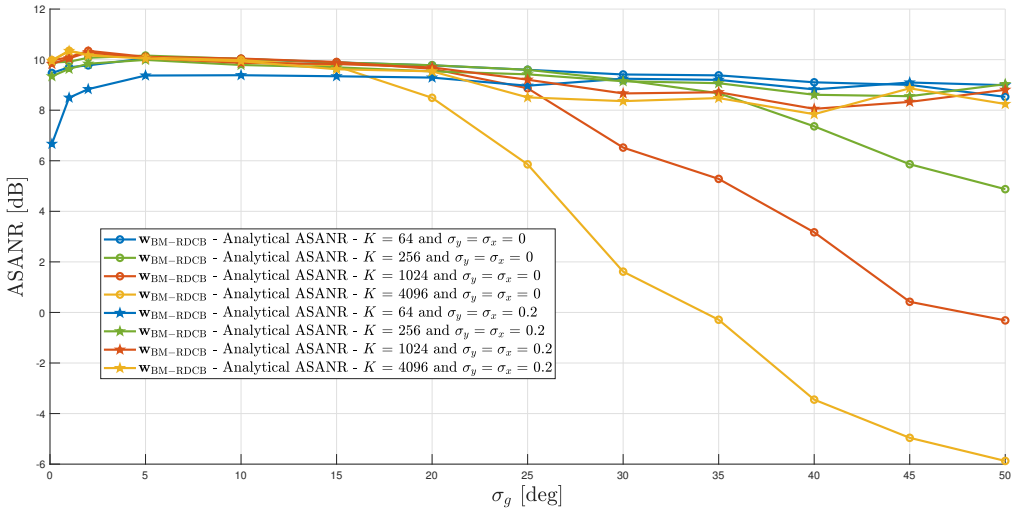

Figure 18. Performance evaluation of the proposed $\mathbf{w}_{\mathrm{BM-RDCB}}$ in terms of the analytical ASANR vs. the angular spread in dual-hop bichromatic–monochromatic scenarios for $K = 64, 256, 1024, 4096$; $d/\lambda = 0.5$; and $\sigma_x = \sigma_y = 0, 0.2$.

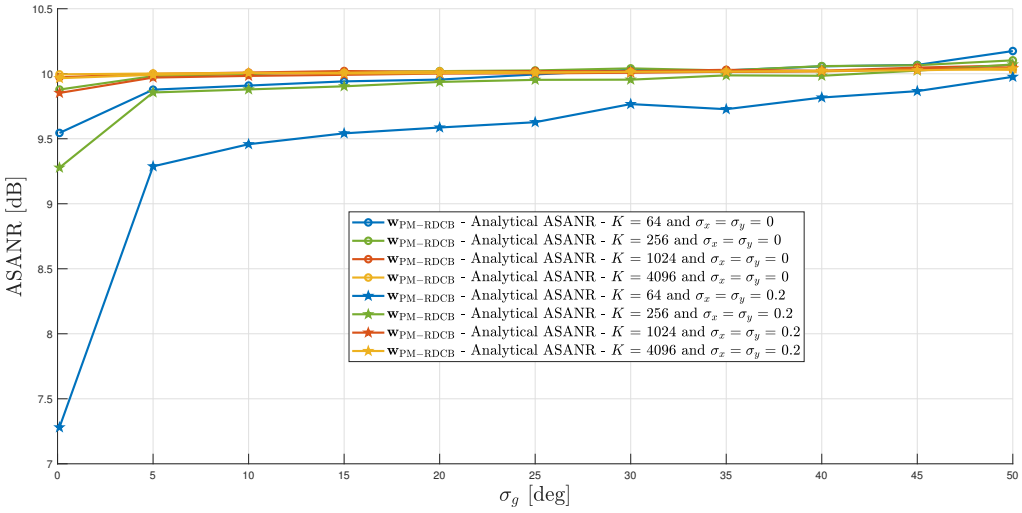

Figure 19. Performance evaluation of the proposed $\mathbf{w}_{\mathrm{PM-RDCB}}$ in terms of the analytical ASANR vs. the angular spread in dual-hop polychromatic–monochromatic scenarios for $K = 64, 256, 1024, 4096$; $d/\lambda = 0.5$; and $\sigma_x = \sigma_y = 0, 0.2$.

5. Conclusions

We introduce an RDCB solution designed to address significant channel estimation issues in dual-hop transmissions across a wireless sensor and actuator network (WSAN) with K nodes arranged in a nominally rectangular or square layout. The process begins with the source S transmitting its signal to the WSAN. WSANs achieve higher efficiency in wireless communications by minimizing data transmission, reducing latency, conserving energy, and optimizing network loads through the integration of both sensing and actuation capabilities. Next, the process continues with each node then forwarding its received signal to the destination D after applying a selected beamforming weight to minimize the noise power while ensuring a distortionless response to the desired signal at the destination D. These weights rely on CSI parameters, necessitating local estimation or feedback at each node. However, such estimation or feedback may introduce errors, which can degrade the performance of DCB. In light of the extensive connectivity offered by emerging 5G and

future 5G+/6G technologies, along with the IoT, we propose alternative RDCB strategies that are adaptable to various propagation scenarios—monochromatic (line-of-sight or no AS), bichromatic (slightly to moderately scattered or small to medium AS values), and polychromatic (highly scattered or large AS values)—during the first hop, with an LoS link assumed for the second hop. These solutions are designated as MM-RDCB, BM-RDCB, and PM-RDCB, respectively. Our methodology utilizes highly efficient asymptotic approximations for a large number of nodes, K, and exploits the geometric symmetries present in their rectangular or square configurations. Furthermore, the MM-RDCB, BM-RDCB, and PM-RDCB solutions are designed to be distributed, enabling each terminal to locally compute its weights. This significantly enhances both spectral and power efficiency within the WSAN. Our RDCB approach enhances robustness by mitigating CSI estimation errors without high computational costs. It improves computational efficiency through asymptotic approximations, making it ideal for large-scale WSANs, and ensures scalability by leveraging WSAN structures. Simulation results indicated notable improvements in the SNR and increased resilience to errors in node placement. Future research directions include the following: (1) addressing additional scenarios and imperfections (such as phase jitter and interference from external sources), as summarized in Table 4, while shifting the performance evaluation focus from SNR gains to link- and system-level throughput, which will involve incorporating the overhead from inter-node communications and any source- and/or destination-nodes' feedback; (2) exploring new challenges such as the use of Reconfigurable Intelligent Surface (RIS) and unmanned aerial vehicle (UAV) communications; (3) computing closed-form solutions in multi-source environments; and (4) pursuing hardware prototyping, experimental validation, and real-time performance evaluation for the new RDCB designs in realistic conditions, including testing in over-the-air and real-time scenarios.

Table 4. Applicable scenarios for single-source RDCB in terms of dual-hop communication scenarios (backward/forward channels vs. rows/columns or vice versa due to reciprocity between *S*-WSAN-*D* and *D*-WSAN-*S* links).

Dual-Hop Channels	Unstructured	Monochromatic	Bichromatic	Polychromatic
Unstructured	N.A.	Ongoing	Ongoing	Ongoing
Monochromatic	Ongoing	✓ (this work)	✓ (this work)	✓ (this work)
Bichromatic	Ongoing	✓ (this work)	Ongoing	Ongoing
Polychromatic	Ongoing	✓ (this work)	Ongoing	Ongoing

Author Contributions: Conceptualization, O.B.S. and S.A.; Funding acquisition, S.A.; Investigation, O.B.S.; Methodology, O.B.S.; Project administration, S.A.; Resources, S.A.; Software, O.B.S.; Supervision, S.A.; Validation, O.B.S., S.A., D.J. and Y.N.; Writing—original draft, O.B.S.; Writing—review and editing, S.A., D.J. and Y.N. All authors have read and agreed to the published version of the manuscript.

Funding: This work was supported by the Discovery Grants (DGs) and CREATE PERSWADE (<www.create-perswade.ca>) Programs of NSERC.

Data Availability Statement: The raw data supporting the conclusions of this article will be made available by the authors on request.

Conflicts of Interest: The authors declare no conflicts of interest. The funders had no role in the design of the study; in the collection, analyses, or interpretation of data; in the writing of the manuscript; or in the decision to publish the results.

Appendix A

In dual-hop polychromatic–monochromatic propagation scenarios, the optimal CB solution given in (11) takes the following form:

$$\bar{\mathbf{w}}_{\mathrm{PM-DCB}} = \frac{\bar{\mathbf{\Lambda}}^{-1}\bar{\mathbf{h}}}{\sum_{l,m=1}^{L}\alpha_l^*\alpha_m\frac{\sin\left(\frac{K_2P_{2,l,m}}{2}\right)}{\sin\left(\frac{P_{2,l,m}}{2}\right)}\left(1+2\frac{\sin\left(\frac{K_1-1}{4}P_{1,l,m}\right)}{\sin\left(\frac{P_{1,l,m}}{2}\right)}\exp\left(j\frac{K_1+1}{4}P_{1,l,m}\right)\right)}, \quad \text{(A1)}$$

where $P_{1,l,m} = \frac{2\pi d_1}{\lambda}[\cos(\phi_l) - \cos(\phi_m)]$ and $P_{2,l,m} = \frac{2\pi d_2}{\lambda}[sin(\phi_l) - \sin(\phi_m)]$ for $\{l,m\} \in \{1,2,\ldots,L\}$.

In dual-hop bichromatic–monochromatic propagation scenarios, the optimal CB solution in (11) simplifies to the following form:

$$\bar{\mathbf{w}}_{\mathrm{BM-DCB}} = \frac{\bar{\mathbf{\Lambda}}^{-1}\bar{\mathbf{h}}}{K(\rho_1^2+\rho_2^2)+2K_1\rho_1\rho_2\cos(\theta_1-\theta_2)\Pi(K_2)}, \quad \text{(A2)}$$

where

$$\begin{aligned}\Pi(K_2) &= \sum_{q=1}^{K_2}\cos\left(\frac{4\pi d_2}{\lambda}\sin(\sigma_{\mathbf{g}})\left(q-\frac{K_2+1}{2}\right)\right)\\ &= \begin{cases}\dfrac{\sin\left(\frac{K_2\frac{4\pi d_2}{\lambda}\sin(\sigma_{\mathbf{g}})}{2}\right)}{\sin\left(\frac{\frac{4\pi d_2}{\lambda}\sin(\sigma_{\mathbf{g}})}{2}\right)}, & \text{if } \exp\left(j\frac{4\pi d_2}{\lambda}\sin(\sigma_{\mathbf{g}})\right)\neq 1\\ K_2, & \text{otherwise.}\end{cases}\end{aligned} \quad \text{(A3)}$$

In dual-hop monochromatic–monochromatic propagation scenarios, the formulation in (11) simplifies to the following DCB beamformer:

$$\bar{\mathbf{w}}_{\mathrm{MM-DCB}} = \frac{\bar{\mathbf{\Lambda}}^{-1}\bar{\mathbf{h}}}{K}. \quad \text{(A4)}$$

Appendix B

The expressions of $\Xi_{\star M}$ with $\star \in \{\mathrm{P},\mathrm{B},\mathrm{M}\}$ for large values of K in dual-hop polychromatic–monochromatic, bichromatic–monochromatic, and monochromatic–monochromatic propagation scenarios, respectively, are given by the following expressions:

$$\Xi^2_{PM}(K_1,K_2,d_1,d_2,\sigma_x,\sigma_y,\alpha_i,\phi_i,\Phi_D)=\lim_{K\to\infty}\left|\bar{\mathbf{h}}^H\bar{\mathbf{\Lambda}}^{-1}\mathbf{h}\right|^2=$$
$$\sum_{l,m,n,o=1}^{L}\alpha_l\alpha_m^*\alpha_n^*\alpha_o\Big[\operatorname{sinc}((P_{3,l,D}-P_{3,n,D})\sqrt{3}\sigma_x)\operatorname{sinc}((P_{4,l,D}-P_{4,n,D})\sqrt{3}\sigma_y)$$
$$\times\frac{\sin\left(\frac{K_2(P_{2,l,m}-P_{2,n,o})}{2}\right)}{\sin\left(\frac{P_{2,l,m}-P_{2,n,o}}{2}\right)}\left(1+2\frac{\sin\left(\frac{(K_1-1)(P_{1,l,m}-P_{1,n,o})}{4}\right)}{\sin\left(\frac{P_{1,l,m}-P_{1,n,o}}{2}\right)}\exp\left(j\frac{K_1+1}{4}(P_{1,l,m}-P_{1,n,o})\right)\right)$$
$$+\operatorname{sinc}(P_{3,l,D}\sqrt{3}\sigma_x)\operatorname{sinc}(P_{3,n,D}\sqrt{3}\sigma_x)\operatorname{sinc}(P_{4,l,D}\sqrt{3}\sigma_y)\operatorname{sinc}(P_{4,n,D}\sqrt{3}\sigma_y)$$
$$\times\left(\frac{\sin\left(\frac{K_2}{2}P_{2,l,m}\right)}{\sin\left(\frac{P_{2,l,m}}{2}\right)}\frac{\sin\left(\frac{K_2}{2}P_{2,n,o}\right)}{\sin\left(\frac{P_{2,n,o}}{2}\right)}\left(1+2\frac{\sin\left(\frac{(K_1-1)P_{1,l,m}}{4}\right)}{\sin\left(\frac{P_{1,l,m}}{2}\right)}\exp\left(j\frac{K_1+1}{4}P_{1,l,m}\right)\right)\right.$$
$$\times\left(1+2\frac{\sin\left(\frac{(K_1-1)P_{1,n,o}}{4}\right)}{\sin\left(\frac{P_{1,n,o}}{2}\right)}\exp\left(j\frac{K_1+1}{4}P_{1,n,o}\right)\right)-\frac{\sin\left(\frac{K_2(P_{2,l,m}-P_{2,n,o})}{2}\right)}{\sin\left(\frac{P_{2,l,m}-P_{2,n,o}}{2}\right)}$$
$$\left.\times\left(1+2\frac{\sin\left(\frac{(K_1-1)(P_{1,l,m}-P_{1,n,o})}{4}\right)}{\sin\left(\frac{P_{1,l,m}-P_{1,n,o}}{2}\right)}\exp\left(j\frac{K_1+1}{4}(P_{1,l,m}-P_{1,n,o})\right)\right)\right)\Big]. \tag{A5}$$

$$\Xi^2_{BM}(K_1,K_2,d_1,d_2,\sigma_x,\sigma_y,\sigma_g,\rho_1,\rho_2,\theta_1,\theta_2,\Phi_D)=\lim_{K\to\infty}\left|\bar{\mathbf{h}}^H\bar{\mathbf{\Lambda}}^{-1}\mathbf{h}\right|^2=$$
$$K(\rho_1^2+\rho_2^2)^2+2K\rho_1^2\rho_2^2C_{y_1}+2\rho_1\rho_2(\rho_1^2+\rho_2^2)\cos(\theta_1-\theta_2)K_1B(A)(C_{y_1}+1)+K_1B(2A)C_{y_1}$$
$$\times(2\rho_1^2\rho_2^2\cos(2(\theta_1-\theta_2)))+C_x^2\Big[K(K-1)(\rho_1^2C_{y_2}+\rho_2^2C_{y_3})^2+G(A)(2\rho_1\rho_2\cos(\theta_1-\theta_2)$$
$$\times\left(\rho_1^2C_{y_2}^2+\rho_2^2C_{y_3}^2+(\rho_1^2+\rho_2^2)C_{y_2}C_{y_3}\right))+E(A)(2\rho_1^2\rho_2^2\cos(2(\theta_1-\theta_2))C_{y_2}C_{y_3})$$
$$+F(A)\rho_1^2\rho_2^2\left(C_{y_2}^2+C_{y_3}^2\right)\Big] \tag{A6}$$

$$\Xi^2_{MM}(K,d_1,d_2,\sigma_x,\sigma_y,\Phi_D)=\lim_{K\to\infty}\left|\bar{\mathbf{h}}^H\bar{\mathbf{\Lambda}}^{-1}\mathbf{h}\right|^2=$$
$$K+K(K-1)\frac{\sin\left(\frac{2\pi d_1(1+\cos(\phi_D))}{\lambda}\sqrt{3}\sigma_x\right)^2}{\left(\frac{2\pi d_1(1+\cos(\phi_D))}{\lambda}\sqrt{3}\sigma_x\right)^2}\frac{\sin\left(\frac{2\pi d_2\sin(\phi_D)}{\lambda}\sqrt{3}\sigma_y\right)^2}{\left(\frac{2\pi d_2\sin(\phi_D)}{\lambda}\sqrt{3}\sigma_y\right)^2}. \tag{A7}$$

We define in (A5) and (A6) the following terms:

$$
\begin{aligned}
P_{3,l,D} &= \frac{2\pi d_1}{\lambda}[\cos(\phi_l) + \cos(\phi_D)] \quad \text{for } l \in \{1, 2, \ldots, L\}, \\
P_{4,l,D} &= \frac{2\pi d_2}{\lambda}[\sin(\phi_l) + \sin(\phi_D)] \quad \text{for } l \in \{1, 2, \ldots, L\}, \\
A &= \frac{4\pi d_2}{\lambda}\sin(\sigma_g), \\
C_x &= \operatorname{sinc}\left(\frac{2\pi d_1}{\lambda}[\cos(\sigma_g) + \cos(\phi_D)]\sqrt{3}\sigma_x\right), \\
C_{y_1} &= \operatorname{sinc}\left(A\sqrt{3}\sigma_y\right), \\
C_{y_2} &= \operatorname{sinc}\left(\frac{2\pi d_2}{\lambda}[\sin(\sigma_g) + \sin(\phi_D)]\sqrt{3}\sigma_y\right), \\
C_{y_3} &= \operatorname{sinc}\left(\frac{2\pi d_2}{\lambda}[\sin(\phi_D) - \sin(\sigma_g)]\sqrt{3}\sigma_y\right), \\
B(A) &= \frac{\sin(K_2 A/2)}{\sin(A/2)}, \\
E(A) &= K_1^2 B(A)^2 - K_1 B(2A), \\
F(A) &= K_1^2 B(A)^2 - K, \\
G(A) &= K K_1 B(A) - K_1 B(A).
\end{aligned}
$$

References

1. Janardhan, N.; Nandhini, K. Wireless Sensor and Actuator Networks (WSANs): Insights and Scope of Research. *Int. J. Innov. Technol. Explor. Eng.* **2019**, *8*, 1607–1615. [CrossRef]
2. Ngai, E. C.; Lyu, M. R.; Liu, J. A Real-Time Communication Framework for Wireless Sensor-Actuator Networks. In Proceedings of the IEEE Aerospace Conference 2006, Big Sky, MT, USA, 4–11 March 2006.
3. Verdone, R.; Dardari, D.; Mazzini, G.; Conti, A. *Wireless Sensor and Actuator Networks: Technologies, Analysis and Design*; Academic Press: Cambridge, MA, USA, 2010.
4. Xia, F. QoS Challenges and Opportunities in Wireless Sensor/Actuator Networks. *Sensors* **2008**, *8*, 1099–1110. [CrossRef] [PubMed]
5. Ben Smida, O.; Zaidi, S.; Affes, S.; Valaee, S. Robust Distributed Collaborative Beamforming for Wireless Sensors Networks with Channel Parameter Estimation Errors. *Sensors* **2019**, *19*, 1061. [CrossRef] [PubMed]
6. Huang, J.; Wang, P.; Wan, Q. Collaborative Beamforming for Wireless Sensor Networks with Arbitrary Distributed Sensors. *IEEE Commun. Lett.* **2012**, *16*, 1118–1120. [CrossRef]
7. Zou, J.; Sun, S.; Masouros, C.; Cui, Y.; Liu, Y.F.; Ng, D.W.K. Energy-Efficient Beamforming Design for Integrated Sensing and Communications Systems. *IEEE Trans. Commun.* **2024**, *72*, 3766–3782. [CrossRef]
8. Zarifi, K.; Zaidi, S.; Affes, S. A Distributed Amplify-and-Forward Beamforming Technique in Wireless Sensor Networks. *IEEE Trans. Sig. Proc.* **2011**, *59*, 3657–3674. [CrossRef]
9. Zaidi, S.; Affes, S. Distributed Collaborative Beamforming in the Presence of Angular Scattering. *IEEE Trans. Commun.* **2014**, *462*, 1668–1680. [CrossRef]
10. Zaidi, S.; Affes, S. Distributed Collaborative Beamforming Design for Maximized Throughput in Interfered and Scattered Environments. *IEEE Trans. Commun.* **2015**, *63*, 4905–4919. [CrossRef]
11. Zaidi, S.; Affes, S. SNR and Throughput Analysis of Distributed Collaborative Beamforming in Locally-Scattered Environments. *Wirel. Commun. Mob. Comp.* **2012**, *12*, 1620–1633. [CrossRef]
12. Zaidi, S.; Ben Smida, O.; Affes, S.; Valaee, S. Distributed Zero-Forcing AF Beamforming for Energy-Efficient Communications in Networked Smart Cities. In Proceedings of the IEEE PIMRC 2017, Montreal, QC, Canada, 8–13 October 2017.
13. Ouassal, H.; Yan, M; Nanzer, J.A. Decentralized Frequency Alignment for Collaborative Beamforming in Distributed Phased Arrays. *IEEE Trans. Wirel. Commun.* **2021**, *20*, 6269–6281. [CrossRef]
14. Mirzaei, A.; Zandiyan, S. A Novel Approach for Establishing Connectivity in Partitioned Mobile Sensor Networks using Beamforming Techniques. *arXiv* **2023**, arXiv:2308.04797. [CrossRef]
15. He, M.; Chen, Y.; Liu, M.; Fan, X.; Zhu, Y. Reliable and Energy-Efficient Communications in Mobile Robotic Networks by Collaborative Beamforming. *ACM Trans. Sens. Netw.* **2024**, *20*, 1–24. [CrossRef]

16. Chen, P.; Yang, Y.; Wang, Y.; Ma, Y. Robust Adaptive Beamforming with Sensor Position Errors Using Weighted Subspace Fitting-Based Covariance Matrix Reconstruction. *Sensors* **2018**, *18*, 1476. [CrossRef] [PubMed]
17. Wang, R.; Jiang, Y.; Zhang, W. A Distributed MIMO Relay Scheme Inspired by Backpropagation Algorithm. In Proceedings of the 2021 IEEE Global Communications Conference (GLOBECOM), Madrid, Spain, 7–11 December 2021; pp. 1–6.
18. Jafri, M.; Anand, A.; Srivastava, S.; Jagannatham, A.K.; Hanzo, L. Robust Distributed Hybrid Beamforming in Coordinated Multi-User Multi-Cell Mmwave MIMO Systems Relying on Imperfect CSI. *IEEE Trans. Commun.* **2022**, *70*, 8123–8137. [CrossRef]
19. Ab Majid, N.I.; Abd Malik, N.N.N.; Zakaria, N.A. Node Positioning Error Optimization for Collaborative Beamforming in Wireless Sensor Network. In Proceedings of the IEEE International Symposium on Antennas and Propagation (ISAP), Kuala Lumpur, Malaysia, 30 October–2 November 2023; pp. 1–2.
20. Yang, Z.; Jiang, B. Robust Adaptive Beamforming Based on Covariance Matrix Reconstruction and SV Estimation. In Proceedings of the Second International Conference on Electronic Information Engineering and Computer Communication (EIECC 2022), Xi'an, China, 25–27 November 2022; SPIE: Bellingham, WA, USA, 2023; Volume 12594, pp. 577–583.
21. Mohammadzadeh, S.; Nascimento, V.H.; de Lamare, R.C.; Kukrer, O. Study of Robust Adaptive Beamforming with Covariance Matrix Reconstruction Based on Power Spectral Estimation and Uncertainty Region. *arXiv* **2023**, arXiv:2304.10502.
22. Luo, Z.; Hu, Y.; Liu, H.; Li, Y. Robust Hybrid Beamforming Designs for Full-Duplex OFDM Millimeter Wave Systems with Imperfect Channel Estimates. *Digit. Signal Process.* **2023**, *133*, 103878. [CrossRef]
23. Savas, Y.; Noorani, E.; Koppel, A.; Baras, J.; Topcu, U.; Sadler, B.M. Collaborative One-Shot Beamforming under Localization Errors: A Discrete Optimization Approach. *Sig. Proc.* **2022**, *200*, 108647. [CrossRef]
24. Ben Smida, O.; Zaidi, S.; Affes, S.; Valaee, S. Low-Cost Robust Distributed Collaborative Beamforming against Implementation Impairments. In Proceedings of the IEEE GLOBECOM 2018, Abu Dhabi, United Arab Emirates, 9–13 December 2018.
25. Iqbal, M.; Ashraf, T.; Ahmad, A.; Sohaib, S.; Pan, J.Y.; Lee, S.S. Distributed Beamforming using Trial and Error Learning Algorithm. In Proceedings of the IEEE APCC 2021, Kuala Lumpur, Malaysia, 10–13 October 2021; pp. 275–280.
26. Ruan, H.; de Lamare, R.C. Distributed Robust Beamforming based on Low-Rank and Cross-Correlation Techniques: Design and Analysis. *IEEE Trans. Signal Process.* **2019**, *67*, 6411–6423. [CrossRef]
27. Havary-Nassab, V.; Shahbazpanahi, S.; Grami, A.; Luo, Z.Q. Distributed Beamforming for Relay Networks based on Second-Order Statistics of the Channel State Information. *IEEE Trans. Sig. Proc.* **2008**, *56*, 4306–4316. [CrossRef]
28. Morrison, W.J.; Humphreys, T.E.; Ton-Nu, D.A. Robust Beampattern Synthesis for UAV-Swarm-Based Distributed Beamforming. In Proceedings of the 37th International Technical Meeting of the Satellite Division of the Institute of Navigation (ION GNSS+), Baltimore, MD, USA, 16–20 September 2024; pp. 2754–2765.
29. Yan, J. *Machinery Prognostics and Prognosis Oriented Maintenance Management*; John Wiley & Sons: Hoboken, NJ, USA, 2014.
30. Yick, J.; Biswanath, M.; Dipak, G. Wireless Sensor Network Survey. *Comput. Netw.* **2008**, *12*, 2292–2330. [CrossRef]
31. Ben Smida, O.; Affes, S. Dual-Hop Robust Distributed Collaborative Beamforming Over Nominally Rectangular WSNs in Slightly to Moderately Scattered Environments: (Invited Paper). In Proceedings of the IEEE IWCMC 2023, Marrakesh, Morocco, 19–23 June 2023.
32. Souden, M.; Affes, S.; Benesty, J. A Two-Stage Approach to Estimate the Angles of Arrival and the Angular Spreads of Locally Scattered Sources. *IEEE Trans. Signal Process.* **2008**, *56*, 1968–1983. [CrossRef]
33. Affes, S.; Gazor, S.; Grenier, Y. An Algorithm for Multisource Beamforming and Multitarget Tracking. *IEEE Trans. Signal Process.* **1996**, *44*, 1512–1522. [CrossRef]